The actin nucleator Spire cooperates with Rab11 to initiate nascent dendrite branches.

Authors: Deirdre Hatton[1,2,3,5], Claire Marquilly[1,2,5], Caitlin Hanrahan[1,2,3], Tiago Ferreira[1,2], Yimiao Ou[1,2], Will Silkworth[4], Margot Quinlan[4], Donald J. van Meyel[1,2,6].

Affiliations: [1]Centre for Research in Neuroscience, Department of Neurology and Neurosurgery, McGill University, Montreal, Quebec, Canada.

[2]Research Institute of the McGill University Health Centre, Montreal, Quebec, Canada

[3]Integrated Program in Neuroscience, McGill University, Montreal, Quebec, Canada

[4] University of California Los Angeles, Dept. of Chemistry and Biochemistry, Los Angeles, CA

[5] These authors contributed equally.

[6] Lead contact.

Correspondence: don.vanmeyel@mcgill.ca

Abstract

Dendrites form arbors whose size, shape and complexity define how neurons cover their receptive territories. Actin dynamics contribute to growth and remodelling of dendrite arbors. Here we examined how Spire, a conserved actin nucleation factor, promotes formation of new branches in vivo. In live imaging of Drosophila class IV dendritic arborisation (c4da) neurons, Spire was observed at new sites of branch initiation, where it assembled new actin polymer prior to filopodial outgrowth. For dendrite arborization, Spire required intact structural domains to nucleate actin and target the secretory network, and Spire interacted with Rab11 GTPase, a key regulator of recycling endosomes. Together, these findings support a model that Spire cooperates with Rab11 to promote new dendrite branches by linking localized actin assembly with intracellular trafficking of endosomes that deliver lipids and cargoes to fuel protrusive outgrowth of nascent dendrites.

Keywords: dendrite, neuron, development, nervous system, actin, Drosophila, endomembrane system, secretory network, recycling endosome

Introduction

Different types of neurons are characterized by dendrites with distinct tree-like branching patterns that influence the number, strength, and integration of sensory or synaptic inputs into neurons (Grueber et al., 2005; Lefebvre et al., 2015; London and Hausser, 2005). A major gap remains in our understanding of the spatiotemporal control of cytoskeletal remodelling responsible for dendrite morphogenesis during development (Lefebvre, 2021). Understanding how dendrites are shaped during development is essential to gain full insight into the construction of neural circuits that underlie animal survival, behaviors, learning, and

memory (Luo, 2021). The growth and structural remodelling of dendrite arbors requires complex spatial and temporal regulation of actin dynamics (Konietzny et al., 2017), involving coordination of specific proteins to nucleate and elongate actin filaments (Rottner et al., 2017; Siton-Mendelson and Bernheim-Groswasser, 2017). Furthermore, to cope with their size and complexity, dendrites have specialized arrangements of secretory network organelles for the biogenesis of cargo-carrying vesicles and their transport to the cell surface (Kennedy and Hanus, 2019). Given the importance of actin and the secretory network for dendrite development and function, it is important to clarify how they are coordinated to initiate new dendrite branches in vivo (Lanoue and Cooper, 2019; Lefebvre, 2021).

New dendrite branches arise from actin-rich filopodia that rapidly extend from initiation sites along established branches (Lanoue and Cooper, 2019). Dendrite filopodia are structurally distinct from conventional filopodia, with an unusual network-like cytoskeletal organization characterized by both branched and linear filaments of mixed polarity (Korobova and Svitkina, 2010), suggesting involvement of multiple actin regulatory proteins with distinct activities. Few studies have identified specific actin regulators involved in forming new branches (Hou et al., 2015; Nithianandam and Chien, 2018; Shi et al., 2021; Sturner et al., 2022; Sturner et al., 2019; Zou et al., 2018), and none have pinpointed their regulation of actin to the location and timing of nascent branch outgrowth. In sensory neurons of living Drosophila larvae, the locations of dendrite filopodia initiation sites are pre-figured by patches of actin polymer (Andersen et al., 2005; Nithianandam and Chien, 2018; Sturner *et al.*, 2019), as has been proposed for dendrite filopodia in the mouse brain also (Willig et al., 2014). In Drosophila larvae, class IV dendritic arborization (c4da) neurons provide an excellent model to study the roles of actin regulators in the development of dendrite arbors in vivo (Grueber et al., 2002; Medina et al., 2006; Nagel et al., 2000). In c4da neurons, formation of new dendrites requires the Arp2/3 actin nucleator complex under control of the activator WAVE and the small GTPase

Rac1 (Sturner *et al.*, 2019). New dendrite formation also involves F-actin severing by Twinstar/Cofilin in the production of "blobs" of pre-assembled actin polymer, which move bidirectionally within dendrites, pause before filopodium outgrowth, and appear to contribute F-actin into the nascent branch (Nithianandam and Chien, 2018). It is unclear whether stationary actin patches and motile actin blobs are features of convergent or parallel processes to initiate dendrite branches (Pai and Moore, 2018). Moreover, the factor(s) that specify the location and timing of filopodial outgrowth from actin patches and blobs have not been defined.

Here we explored the role of Spire (Spir), a conserved multi-domain actin nucleation factor. We previously showed that knockdown of Spir with RNA interference (RNAi) in cd4da neurons led to reduced number of terminal dendrite branches and compromised the ability of these nociceptive neurons to elicit larval escape from noxious stimulus (Ferreira et al., 2014a). Spir is known to co-operate with Fmn-family formins, which are also actin nucleators, during Drosophila and mouse oogenesis (Manseau and Schupbach, 1989; Pfender et al., 2011; Quinlan et al., 2005; Vizcarra et al., 2011). Spir has four WASP homology 2 (WH2)-domains for actin nucleation, a KIND domain for interaction with Capu/Fmn, a modified FYVE (mFYVE) domain to target vesicles of the secretory network, and a SPIR-box with potential to interact with Rab GTPases (Kerkhoff et al., 2001; Quinlan *et al.*, 2005; Quinlan et al., 2007; Tittel et al., 2015), which play roles in vesicle sorting and transport (Kiral et al., 2018). Our findings indicate that Spir stimulates new actin polymer just prior to filopodial outgrowth and that Spir cooperates with Rab11 to promote new dendrite branches, supporting a model in which Spir and Rab11 link localized actin assembly with recycling endosomes that deliver lipids and cargoes to nascent dendrites.

Results

74 **Spir is required for localized F-actin synthesis just prior to outgrowth of new dendrite**
75 **branches.**

76 The development of Drosophila c4da neuron dendrites begins in embryogenesis and
77 continues in larval stages, with arbors growing in the larval body wall between muscles and
78 epithelial cells (Grueber *et al.*, 2002). To reveal actin dynamics leading up to the protrusion of
79 dendrite filopodia, we acquired time-lapse movies (5 minutes (min) each) in second instar (L2)
80 larvae, capturing F-actin (labeled with LifeAct::GFP) within c4da neurons (labeled with ppk-
81 CD4::tdTom) (Fig. 1A, B). In control animals (+/+ and $spir^{2F}$/+ heterozygotes) LifeAct::GFP
82 was seen in stationary puncta that appeared *de novo* at the site shortly before initiation (Fig.
83 1A) or in pre-formed actin blobs that moved to the branching site prior to branch initiation (Fig.
84 1B). Instances where a new filopodium grew from a site where an actin punctum existed in the
85 first frame of the movie were disregarded because the movie did not capture the origin of the
86 actin punctum. Like the LifeAct::GFP signal that arose de novo at branch initiation points, the
87 LifeAct::GFP signal from pre-formed actin blobs became more intense just prior to branch
88 initiation and then, upon outgrowth, LifeAct::GFP signal extended into the protruding nascent
89 branchlet (Fig. 1A, B). The intensity increase of LifeAct::GFP was specific to branch initiation
90 points; it did not occur at nearby puncta.

91 To confirm expression of the actin nucleator Spir in c4da neurons, we produced a *GAL4*
92 line inserted in the *spir* locus ($spir^{GAL4}$) and used it to drive *UAS-mCD8::GFP*, which encodes
93 a fluorescent reporter targeted to the plasma membrane. $spir^{GAL4}$ was expressed in c4da neurons
94 marked by ppk-CD4::tdTom and other sensory neurons in the larval body wall (Fig. 1C). We
95 confirmed this using immunohistochemistry (IHC) with newly generated anti-Spir sera (Fig.
96 S1A), consistent with our previous research (Ferreira *et al.*, 2014a).

97 To study how complete loss of *spir* affects actin accumulation and dendrite
98 arborization, we examined $spir^{1}$ and $spir^{2F}$ mutants, which harbor point mutations causing
99 premature stop codons predicted to truncate the Spir protein within the KIND domain (Fig.
100 1D) (Wellington et al., 1999). We studied these mutant alleles in combination with a deficiency
101 ($spir^{Df}$) to control for effects of genetic background in homozygotes. Using antiserum directed
102 to an epitope C-terminal to these mutations, we confirmed that *spir* mutants lack Spir
103 expression with IHC in larval sensory neurons (Fig. S1A), and with western blot analysis of
104 adult brain lysates (Fig. S1B). In *spir* mutants, overall levels of LifeAct::GFP expression in
105 dendrites appeared lower than in controls, consistent with our previous observations upon Spir
106 knockdown with RNAi (Ferreira *et al.*, 2014a). However, the LifeAct::GFP signal remained
107 strong enough to monitor actin at sites of new branch initiation with time-lapse imaging.
108 In contrast to controls, in $spir^{2F}/spir^{Df}$ mutant larvae we observed no instances where
109 actin polymer appeared *de novo* prior to branch initiation (Fig. 1F). All new dendrite filopodia
110 stemmed from pre-formed actin blobs that moved to the initiation site (Fig. 1E). We measured
111 LifeAct::GFP fluorescence intensity at branch initiation sites. In controls (+/+) the signal in
112 both actin blobs and stationary actin puncta increased roughly two-fold on average in the 60s
113 prior to outgrowth and remained at the elevated intensity for at least 60s afterward (Fig. 1G).
114 In contrast, in $spir^{2F}/spir^{Df}$ mutants the intensity of LifeAct::GFP in actin blobs did not increase
115 prior to branch initiation or afterward (Fig. 1E,G).
116
117 **Localization of Spir in developing dendrites, and requirement of Spir for new branch**
118 **formation.**
119 Using IHC to examine $spir^{1}$/+ controls, we found that the cell bodies and proximal
120 dendrites of c4da neurons in L3 larvae were immunopositive for Spir (Fig. S1A), but we did
121 not detect Spir in distal dendrites with our new antisera. However, upon over-expressing a

122 *UAS-Spir::GFP* transgene (Fig. 1D) in c4da neurons with *ppk-GAL4,* the anti-Spir serum
123 strongly labelled the cell body and discrete puncta in proximal and distal dendrites (Fig. S1C).
124 The coordinates of Spir::GFP puncta were plotted relative to the skeletonized centerlines of
125 CD4-tdTom labeled dendrites. Spir::GFP puncta were seen in all dendrite shafts, some branch
126 points (28%), but few branch tips (6%) (Fig. S1D,E). Consistent with this, most Spir::GFP
127 puncta were found along dendrite shafts (57%) and at branch points (36%) (Fig. S1F).

128 Time-lapse movies (~1 frame/2 sec for >5 min, L2 larvae) showed a pattern for the GFP
129 tag on Spir::GFP (Fig. 1H) that was like what we observed in fixed L3 larvae (Fig. S1E).
130 Interestingly, some Spir::GFP puncta remained stationary while others were steadily motile or
131 moved in a saltatory manner with occasional pauses (Fig. S1F). Motile puncta were often
132 smaller and rounder, while stationary puncta could be larger and irregular in shape.

133 Every nascent branch we observed in our movies from control larvae (+/+, L2) had a
134 Spir::GFP punctum stationed precisely at (68% of branches) or near (< 1 μm, 32% of branches)
135 the initiation site prior to outgrowth (Fig. 1J). These puncta were seen to arrive from elsewhere
136 (30%, Fig. 1H, K) or were already at that site in the first frame of the movie (70%, Fig. 1I, K).
137 The interval of time from the appearance or arrival of a Spir::GFP punctum at the initiation site
138 until outgrowth showed a broad range (Fig. 1K). Spir::GFP intensity did not typically increase
139 prior to outgrowth but, in some instances (12%), a motile punctum of Spir::GFP combined with
140 one already stationed at the future initiation site. Spir::GFP puncta at or near (< 1 μm) branch
141 initiation sites were stably maintained throughout the process of filopodial outgrowth,
142 stabilization, or retraction, and Spir::GFP signal appeared to invade the filopodia as they grew
143 (Fig. 1I).

144 Terminal branches that existed at the beginning of each movie were monitored for their
145 subsequent dynamics in controls (+/+) and $spir^{2F}/spir^{Df}$ mutants. Neither of these genotypes
146 affected the percentage of pre-existing branches that either extended, retracted, did both, or

147 remained static (Fig. S2A-D). We also compared the protrusive characteristics of nascent
148 branches in instances where actin (labelled with LifeAct::GFP) appeared de novo (seen in +/+
149 only) or after arrival of motile actin blobs (seen in +/+ and *spir*^{2F}/*spir*^{Df} mutants). In both
150 genotypes, typical growth involved saltatory extensions and pauses. There were no differences
151 in the mean speed of outgrowth, the proportion of time spent paused between extensions, or
152 the maximum length of protrusion (Fig. S2E-G).

153 Importantly, the number of terminal dendrites/μm^2 was reduced in *spir*^{2F}/*spir*^{Df} mutants
154 compared to heterozygous controls (Fig. 2A), as quantified per μm^2 in the first frame of each
155 of the time-lapse movies. Based on Spir::GFP localization and because Spir did not exhibit
156 obvious control over the dynamics of pre-existing terminal branches, we focused on new
157 branches. We found that the proportion of new branches formed during each movie was
158 reduced in *spir*^{2F}/*spir*^{Df} mutants (Fig. 2B). Movies of c4da neurons expressing LifeAct::GFP
159 also showed that *spir* mutants had reduced terminal dendrites/μm^2 (Fig S3A), fewer new
160 branches per movie (Fig. S3B), and no effect on branch dynamics (Fig. S3C-F), confirming
161 independently that Spir specifically influences the formation of new branches.

162

163 **Consequences of Spir function for dendrite arborization in c4da neurons.**

164 To explore Spir's role at initiation sites for nascent terminal dendrites, we compared
165 control heterozygotes (*spir*^{2F}/+) to *spir* mutants (*spir*^{2F}/*spir*^{Df}) or *spir* mutants rescued with
166 either Spir::GFP or Spir^{ABCD}::GFP. Spir^{ABCD}::GFP contains a series of 4 triple-alanine
167 substitutions in the WH2 domains that greatly diminish the ability of Spir to polymerize F-
168 actin *in vitro* (Quinlan *et al.*, 2005). In time-lapse movies of L2 larvae, the correct number of
169 terminal dendrites/μm^2 was rescued by expressing intact Spir::GFP in c4da neurons but not by
170 expressing Spir^{ABCD}::GFP (Fig. 2, indicating a role for Spir to establish the correct number of
171 terminal branches that depends on its ability to polymerize F-actin. The proportion of new

172 branches in each movie appeared to be rescued partially by Spir::GFP but also by
173 Spir^{ABCD}::GFP (Fig. 2B). We note the arbors were monitored for only 5 min in these movies,
174 a short window in an arborization process that takes several days. To gain a full view of the
175 effects of Spir on dendrite arborization, we examined images of fully developed c4da arbors in
176 L3 larvae (Fig. 2C), measuring the number of terminal dendrites (Fig. 2D), total arbor length
177 (Fig. 2E), and the area of the dendritic field (Fig. 2F). Compared to heterozygous controls, we
178 found that *spir* mutants (*spir*^{1}/*spir*^{Df} or *spir*^{2F}/*spir*^{Df}) had far fewer terminal branches (Fig. 2D).
179 As perhaps expected with such significant loss of branches, total arbor length was also reduced
180 (Fig. 2E). Dendritic field was not reduced in *spir*^{1}/*spir*^{Df} mutants, but 4 out of the 15 cells in
181 *spir*^{2F}/*spir*^{Df} mutants had fields that were unusually small, and so the average for cells of this
182 genotype was reduced compared to controls (Fig. 2F). When these 4 cells were removed from
183 the analysis to mitigate the potential effect of their small fields, the remaining *spir*^{2F}/*spir*^{Df}
184 mutant cells continued to display far fewer terminal branches than controls (Fig. S4A, B).
185 We also used modified Sholl analysis (Ferreira et al., 2014b; Sholl, 1953) to plot the
186 density profiles of dendrites within an arbor as a function of distance from the cell soma (Fig.
187 2G). The peak of maximum branch density (critical value) was significantly reduced in both
188 *spir*^{1}/*spir*^{Df} and *spir*^{2F}/*spir*^{Df} mutants (Fig. 2H and Fig. S4D). Selective expression of a *UAS-*
189 *Spir::GFP* transgene in c4da neurons with *ppk-GAL4* (Fig. 2C) fully rescued the number of
190 terminal branches in *spir*^{2F}/*spir*^{Df} mutants (Fig. 2D), and the Sholl critical value (Fig. 2H, Fig.
191 S4D). However, Spir::GFP did not fully rescue total arbor length (Fig. 1E, Fig S4C). It is
192 unlikely that incomplete rescue is due to inadequate Spir::GFP expression. Western blots (Fig
193 S1B) and IHC (Fig. S1C) showed the transgene was expressed at similar, and even higher,
194 levels compared to endogenous Spir. Thus, there is a possibility that additional cell types,
195 perhaps the surrounding epidermis or muscle cells of the larval body wall where Spir appeared
196 to be expressed (Fig. S1A, B), contribute to total arbor length. We conclude that Spir acts

197 within c4da neurons to establish the correct number of terminal dendrite branches, likely by
198 initiating the filopodial outgrowth necessary for nascent branches.
199

200 **Each domain of Spir is required for dendrite arborization.**

201 We next sought to determine the importance of the four identified protein domains of
202 Spir by testing if disruptive mutations in Spir::GFP (Fig. 1D) could rescue the correct numbers
203 of terminal branches in c4da neurons of *spir* mutants. In addition to the ABCD mutation in the
204 WH2 domains, we tested Y232K, a missense substitution in the KIND domain known to
205 abolish the interaction between Spir and the formin Cappuccino (Capu) in oocytes (Quinlan,
206 2013; Vizcarra *et al.*, 2011). We also tested ΔSB, a 20 aa deletion of the entire Spir-box domain
207 which has sequence similarity to the Rab effector protein Rabphilin3a suggesting it interacts
208 with Rab GTPases (Kerkhoff *et al.*, 2001). Finally, we tested C5,6S, a substitution of serine
209 residues for 2 key cysteines in the so-called modified FYVE (mFYVE) domain. FYVE
210 domains interact in lipid membranes with Phosphatidylinositol 3-phosphate (PtdIns3P), a
211 prominent component of the membranes in the endosomal system (Marat and Haucke, 2016).
212 The mFYVE domain in Spir binds less specifically to negatively charged lipids, including
213 PtdIns3P, and is required to localize to intracellular membranes (Tittel *et al.*, 2015).

214 The impact of each mutation was determined by expressing the transgenes in c4da
215 neurons (with *ppk-GAL4)* of $spir^{2F}/spir^{Df}$ mutants. Compared with the intact Spir::GFP control,
216 none of these transgenes ($Spir^{Y232K}$::GFP, $Spir^{ABCD}$::GFP, $Spir^{\Delta SB}$::GFP or $Spir^{C5,6S}$::GFP)
217 rescued the number of terminal dendrites per neuron (Fig. 3A), nor the Sholl critical value (Fig.
218 3B, Fig. S5A). When each of these transgenes was expressed in all neurons with *nSyb-GAL4*,
219 western blots of adult head lysates showed that none were expressed at lower levels than intact
220 Spir::GFP (Fig. 3C, D and Fig. S5B), whose levels were clearly enough to support rescue of

221 function. These results demonstrate that each domain contributes to Spir's role in controlling
222 dendrite branching.

223 The effect of each mutation (Y232K, ABCD, ΔSB, or C5,6S) on the distribution of
224 Spir::GFP in c4da neurons was examined in *spir*^{2F}/*spir*^{Df} animals. Spir::GFP was found in
225 puncta at dendrite branch points, shafts and at branch tips (Fig. 3E), as it is in control animals
226 (Fig. 1H and Fig. S1E). None of the Y232K, ABCD, or C5,6S mutations had a dramatic effect
227 on this pattern of distribution (Fig. S5C). In contrast, Spir$^{\Delta SB}$::GFP accumulated near the cell
228 soma and formed a more continuous than punctate pattern (Fig. 3E). Though this might be
229 explained in part by unusually high expression levels (Fig. 3C,D and Fig. S5B), these results
230 suggest that the SB domain is required for proper localization of Spir within c4da arbors.

231

232 **Spir and Rab11 cooperate for dendrite arborization.**

233 The pattern and motility of Spir::GFP puncta within dendrites of c4da neurons was
234 reminiscent of elements of the secretory network, where Rab GTPases including Rab11 and
235 Rab4 are key regulators of vesicle and cargo trafficking (Kiral *et al.*, 2018). Rab11 is associated
236 with the trans-Golgi network, post-Golgi, and recycling endosomes (Sonnichsen et al., 2000).
237 Upon co-expression in c4da neurons, Spir::GFP and Rab11::mCherry appeared to co-localize
238 within dendrites (Fig. 4A). Spir::GFP also appeared to co-label punctae with Rab4-mRFP in
239 dendrites (Fig. S6A), a marker of early endosomes. We focused on Rab11 because previous
240 studies show functional links between Spir and Rab11, in both oocytes and cultured cells
241 (Kerkhoff *et al.*, 2001; Pylypenko et al., 2016; Schuh, 2011). Rab11 is involved in regulated
242 movement of recycling endosomes towards the plasma membrane (Lasiecka and Winckler,
243 2011) and has been shown to traffic receptors and trans-membrane proteins necessary for
244 neurite outgrowth and remodelling (Eva et al., 2010; Park et al., 2004).

245 To test whether Spir and Rab11 can physically associate with one another *in vivo*, Spir-
246 tdTom was co-expressed with either Rab11::GFP or Capu::GFP (a positive control) in all
247 neurons using the *nSyb-GAL4* driver. From lysates of adult heads, co-immunoprecipitation (co-
248 IP) with anti-GFP labelled beads revealed that Spir::tdTom associates (Fig. 4B) with both
249 Rab11::GFP and Capu::GFP but not with Rab6-GFP (negative control, data not shown). This
250 suggests that Spir selectively associates with Rab11 in protein complexes in neurons.

251 We tested whether loss of Rab11 would affect the distribution of Spir::GFP, using *ppk-*
252 *GAL4* to drive the expression of a Rab11-dsRNAi in c4da neurons. Compared to controls (Fig.
253 S6B), knockdown of *Rab11* mRNA in c4da neurons resulted in reduced numbers of branches
254 (Fig. S6C), as published previously (Kramer et al., 2019). However, the distribution of
255 Spir::GFP within arbors was seemingly unaffected by loss of *Rab11* (Fig. S6C), suggesting
256 that Rab11 is not required for Spir localization within c4da neurons.

257 Finally, we used a genetic interaction approach to test whether Spir might operate in
258 the same molecular pathway as Rab11 to control dendrite branching. The arbors of c4da
259 neurons in trans-heterozygotes for mutant alleles of both *spir* and *Rab11* were compared to
260 control heterozygotes for either mutation alone (Fig. 4C). We observed reduced numbers of
261 terminal branches (Fig. 4D) and reduced arbor length (Fig. 4E) only in the trans-heterozygotes
262 but dendritic field was unaffected (Fig. 4F). The Sholl profile also revealed reduced branching
263 (Fig. 4G). Together, these results provide evidence that Spir and Rab11 interact with one
264 another functionally in neurons. We cannot say if the interaction is direct or indirect, but we
265 conclude that they act in a common molecular pathway to regulate dendrite branching.

266

267 **Discussion**

268 We found that Spir promoted the formation of new dendrite branches in vivo by
269 stimulating localized assembly of actin polymer in the seconds leading up to filopodial

outgrowth. Intact domains for actin assembly (KIND, WH2) and for targeting Spir to the secretory network (mFYVE) were essential for Spir function in dendrite arborization. In addition, an intact Spir-box was essential to control the localization and levels of Spir expression in dendrites. The Spir-box has the potential to mediate interactions with Rab GTPases, and here we found physical and genetic interactions to link Spir function with Rab11. Rab11 is a key regulator of recycling endosomes. Together our data indicate that Spir and Rab11 collaborate to stimulate dendrite branch formation. An appealing model is one in which Spir and Rab11 cooperate to deliver lipids and cargoes through the secretory network to fuel protrusive outgrowth of nascent dendrites. Further experiments will be required to test this model.

Newly formed branches in control animals were pre-figured either by the appearance of actin polymer *de novo* or by the arrival of pre-formed actin blobs, in roughly equal proportions. In *spir* mutants, there were fewer new branches, and none stemming from initiation sites with *de novo* actin polymer, indicating that Spir is a critical factor controlling the frequency of new dendrite formation from such sites. Although present and active at initiation sites stemming from pre-formed actin blobs, Spir was dispensable for branch initiation from at least some of them. From this we infer redundancy with other molecular mechanisms for branch initiation, perhaps involving actin synthesized by the Arp2/3 complex which has been shown to transiently localize to branch initiation sites in c4da neurons (Sturner *et al.*, 2019).

Spir::GFP overexpression was not sufficient to induce ectopic branching in the rescue assay (Fig. 2D) nor in +/+ animals (data not shown), and there was a variable interval between the stationing of Spir at a branching site and filopodial outgrowth. These findings suggest that Spir activity is tightly regulated. It may require stoichiometric amounts of additional partners

294 to engage the switch that signals the initiation step. The KIND domain mutation Y232K is
295 known to abolish the interaction between Spir and Capu, and there is some genetic evidence
296 that Spir and Capu interact for dendrite branching in class 3 da (c3da) neurons (Sturner *et al.*,
297 2022), but it remains unclear whether Capu is required in c4da neurons for dendrite
298 arborization. In unpublished data, we built a *capu*^{GAL4} line that did not label c4da neurons, and
299 RNAi lines targeting Capu did not reduce terminal branch number when expressed in c4da
300 neurons. Spir might cooperate with another formin in c4da neurons such as Formin3. Formin3
301 is required for c4da dendrite arborization (Das et al., 2021), and its ortholog INF2 has been
302 reported to interact with mouse Spir-1 in mammalian cells (Manor et al., 2015). It is possible
303 that Spir employs different mechanisms to polymerize actin in dendrites of different neuronal
304 cell types, and further research will be required to identify a partner or determine if Spir could
305 nucleate actin on its own in neurons, as has been shown *in vitro* (Quinlan *et al.*, 2005). It is
306 worth noting that the KIND domain also binds intramolecularly to the mFYVE domain (Tittel
307 *et al.*, 2015). If Spir functions independently of another formin, perhaps the KIND mutation
308 (Y232K) and mFYVE (C5,6S) mutations affect the intramolecular interaction thereby
309 disrupting Spir function in dendrites.

310 It is not known if Spir orthologs are involved in dendrite arborization in mammals, but
311 it is intriguing that mRNA for murine orthologs of Spir (Spir-1 and Spir-2) are expressed in the
312 developing CNS and adult brain (Pleiser et al., 2010; Schumacher et al., 2004). A distinct
313 tandem WH2 domain actin nucleator, Cordon-bleu, has been demonstrated to promote dendrite
314 branch initiation in cultured hippocampal neurons and slice preparations of cerebellar Purkinje
315 neurons (Hou *et al.*, 2015).

316 Why might Spir proteins nucleate localized actin polymer just prior to the emergence
317 of nascent dendrites? Short actin filaments generated by Spir proteins and formins provide

318 tracks for myosin-V motors in long-range, microtubule-independent transport of Rab11-
319 labeled endosomes to the plasma membrane of oocytes (Holubcova et al., 2013; Schuh, 2011)
320 and in dispersal of Rab27a-labeled melanosomes in melanocytes (Alzahofi et al., 2020).
321 Interestingly, the human ortholog of myosin Vb has been shown to bind directly to the
322 orthologs of both Spir and Rab11 (Pylypenko *et al.*, 2016). Similarly, Spir could contribute to
323 an actin pool for myosin-V-mediated delivery of Rab11 vesicles to nascent dendrites, supplying
324 lipids and proteins required for their initiation and protrusive growth. This actin pool could
325 allow for the subsequent invasion of microtubules into these nascent branches, perhaps
326 mediated by myosin-6(Yoong et al., 2020), to enable microtubule-dependent long-distance
327 transport of cargo-carrying vesicles. This idea is consistent with our observation that Spir does
328 not appear to regulate the dynamics or maintenance of pre-existing terminal dendrites in c4da
329 neurons, implicating microtubules and perhaps other actin nucleators in these processes.
330 Further experiments will be required to further elucidate the mechanism and molecular partners
331 relevant to Spir-mediated dendrite branching, and the stimuli that activate Spir function at
332 branch initiation sites in vivo.

333

334 **Acknowledgements**

335 This work was supported by the Canadian Institutes of Health Research (FRN137034 to
336 DJvM), and National Institutes of Health (R01GM096133 to MQ). The authors thank Drs. Greg
337 Emery, Peter McPherson, Martine Girard for advice and sharing reagents, our colleagues
338 Emilie Peco, Eunjoo Cho, Adela Ralbovska, Keith Murai, Sabrina Chierzi and Todd Farmer
339 for helpful suggestions. For technical support, the authors thank Dr. Min Fu and Shi-bo Feng
340 of the RI-MUHC Molecular Imaging Platform, and Tim McLean. Stocks obtained from the
341 Bloomington Drosophila Stock Center (NIH P40OD018537) were used in this study.

342

343 **Author Contributions**

344 M.Q. and D.J.v.M conceived the project and designed experiments with input from all other
345 authors. D.H., C.M., C.H., T.F., Y.O., W.S., performed experiments and analyzed all data.
346 D.J.v.M wrote the manuscript with input from all other authors.

347

348 **Declaration of interests**

349 The authors declare no competing interests.

350

351 **Figure Legends**

352 **Figure 1: Spir is required for localized F-actin synthesis just prior to new branch**
353 **outgrowth.** (A, B) Filmstrips (Supplemental Videos 1 and 2, 1 frame/6.5s) of new dendrite
354 branch formation in a c4da neuron (labeled with ppkCD4::tdTom) of a control (+/+) L2 larva.
355 LifeAct::GFP (driven by *ppk-GAL4*) reveals actin polymer within dendrites, and arrows point
356 to instances where a punctum of F-actin was seen either to appear *de novo* (A) or to pre-exist
357 prior to branch initiation (B). In all instances of either type, LifeAct::GFP signal intensified
358 just prior to branch initiation. Scale bar = 2µm. (C) $spir^{GAL4}$-driven mCD8::GFP in c4da
359 neurons (ppkCD4::tdTom) including ddaC (arrowhead), and other sensory neurons in the body
360 wall of an L3 larva. Scale bar=25µm. (D) Diagram showing Spir protein domains (KIND,
361 WH2, SB, and mFYVE), the locations $spir^{2F}$ and $spir^{1}$ mutations, and the names of the
362 disruptive mutations (Y232K, ABCD, ΔSB, and C5,6S) introduced into Spir::GFP. (E)
363 Filmstrip (Supplemental Video 3, 1 frame/6.5s), showing new dendrite branch formation in a
364 $spir^{2F}/spir^{Df}$ L2 larva. Pre-formed actin polymer (arrow) moved to the initiation site, but

365 LifeAct::GFP signal did not intensify prior to outgrowth. Scale bar = 2μm. (F) Proportion of
366 newly formed terminal branches in L2 larvae that had either *de novo* F-actin or pre-formed F-
367 actin prior to branch initiation in c4da neurons. Graph shows mean ± SEM, comparing controls
368 (+/+, n=50 new branches) with *spir* heterozygotes ($spir^{2F}$/+, n=18 new branches) and *spir*
369 mutants ($spir^{2F}/spir^{Df}$, n=8 new branches). (G) Fold change of F-actin intensity (LifeAct:GFP)
370 at branch initiation sites, from 60s before branch formation to 60s afterward, comparing control
371 (black) and *spir* mutants (red). Graphs (F, G) show mean ± SEM. (H, I) Filmstrips
372 (Supplemental Video 5, 1 frame/~4s and Supplemental Video 6, 1 frame/~7s) of control (+/+)
373 L2 larva, where Spir::GFP (arrows) was observed to move to the initiation site of a new
374 dendrite branch (H), or was already stationed at the site at the beginning of the movie (I). Scale
375 bars = 2μm. (J, K) For newly formed dendrite branches, the distance of the closest Spir::GFP
376 puncta to the site of branch initiation was measured (J), and the time from observation of a
377 stationary Spir::GFP punctum at the site to filopodial outgrowth was recorded (K).

378

379 **Figure 2: Spir is required to initiate new branches within dendrite arbors of c4da**
380 **neurons.** (A, B) Dendrite parameters from time lapse movies of control heterozygotes
381 ($spir^{2F}$/+, n= 10), *spir* mutants ($spir^{2F}/spir^{DF}$, , n= 13, or *spir* mutants rescued with either
382 Spir::GFP (n= 10) or $Spir^{ABCD}$::GFP (n= 8), where graphs show mean ± SEM. Dunnett's test
383 was used for multiple post hoc comparisons, and asterisks in each graph (A, B) indicate
384 significant changes compared to $spir^{2F}$/+ heterozygous controls (**P<0.01, ***P<0.001). (A)
385 Number of terminal branches per μm^2 of area in first frame of each movie. (ANOVA ($F(3, 39)$
386 $= 10.52$, $p < 0.0001$). (B) Proportion of new/total branches in each movie (ANOVA ($F(3,40) =$
387 3.346, $p = 0.0284$). (C) Dendrite arbors of c4da neurons (ddaC) visualized with *ppk-*
388 *CD4::tdTom* in a *spir* heterozygote control (left), a *spir* mutant (middle), and a *spir* mutant
389 rescued with *ppk-Gal4* expressing Spir::GFP (right). (D-H) Dendrite parameters per ddaC

390 neuron in L3 larvae (n=15 for each genotype, graphs show mean ± SEM. Asterisks indicate
391 significant changes compared to *spir*$^{2F/+}$ heterozygous controls. (D) Total number of terminal
392 dendrites per ddaC neuron (ANOVA ($F(4, 70) = 11.30$, $p < 0.0001$). (E) Total length of dendrite
393 arbor (mm) (ANOVA $F(4, 70) = 15.12$, $p < 0.0001$). (F) Dendritic field (mm^2) (ANOVA ($F(4,$
394 $70) = 3.352$, $p = 0.0144$). (G, H) Sholl analysis of entire ddaC neurons labelled with *ppk-*
395 *CD4::tdTom*. (I) Sholl profiles, with dotted line indicating critical value for controls (*spir*$^{2F/+}$)
396 (J) Sholl critical value (ANOVA ($F(4, 70) = 8.936$, $p < 0.0001$).

397

398 **Figure 3: Structure-function to reveal Spir domains required for dendrite arborization**
399 **and Spir localization.** (A-B) Dendrite parameters in L3 larvae, comparing *spir* mutants
400 (*spir*$^{2F/Df}$) with animals rescued with Spir::GFP, or Spir:GFP with domain-specific mutations
401 (n=15 for each genotype, graphs show mean ± SEM). Asterisks indicate significant changes
402 compared to *spir*^{2F}*/Df* mutants. (A) Total number of terminal dendrites per ddaC neuron
403 (ANOVA ($F(5, 83) = 2.269$, $p = 0.0550$). (B) Sholl critical value (ANOVA ($F(5, 84) = 3.552$,
404 $p = 0.058$). (C) Anti-GFP and anti-Actin western blot analysis from adult head lysates.
405 Expected size of Spir::GFP is 142 kDa, and endogenous Actin is 42 kDa. (D) Relative band
406 intensities on western blots (n=3) of Spir::GFP constructs (anti-GFP) normalised to anti-Actin.
407 Spir$^{\Delta SB}$::GFP is present at significantly higher levels than Spir::GFP (Friedman test ($Q (4) =$
408 10.40, $p = 0.0053$), with Dunn's post-hoc tests, where all genotypes were compared to
409 Spir::GFP. (E) *ppk-GAL4*-driven Spir::GFP or Spir$^{\Delta SB}$::GFP in a *spir* mutant background.
410 White boxes in left panels indicate areas magnified in panels to their right. Scale bar=50µm.
411 Compared to the punctate distribution of Spir::GFP in ddaC dendrites, Spir$^{\Delta SB}$::GFP
412 accumulates in a continuous pattern in dendrites proximal to the cell soma (white arrowhead),
413 where GFP expression is also seen to be unusually high.

414

415 **Figure 4. Spire interacts with Rab11 in c4da neurons.** (A) *ppk-GAL4*-driven Spir::GFP and
416 Rab11::mCherry. Cell bodies of ddaC neurons are indicated (white arrowheads). Co-
417 localization is observed at branch points (e.g., orange arrowhead) and dendrite shafts (e.g., blue
418 arrowhead). Scale bar=50µm. (B) Spir::tdTom co-IPs with either Capu::GFP (left) or
419 Rab11::GFP (right) from adult head lysates. (C) Dendrites of c4da neurons labelled with ppk-
420 CD4::tdTom in $spir^{2F}$/+ heterozygotes (left), $Rab11^{Bi}$ heterozygotes (middle), and trans-
421 heterozygotes for both (right). (D-F) Dendrite arbor parameters in *spir* heterozygotes ($spir^{2F}$/+,
422 n=15), *Rab11* heterozygotes ($Rab11^{Bi}$/+, n=17), and trans-heterozygotes ($spir^{2F}$/+; $Rab11^{Bi}$ /+,
423 n=15), where graphs show mean ± SEM. Asterisks indicate significant changes compared to
424 $spir^{2F}$/+ heterozygous controls (*P<0.05). (D) Total number of terminal dendrites (ANOVA
425 (F(2, 44) = 4.745 p = 0.0136). (E) Total length of dendrite arbor (mm) (ANOVA (F(2, 44) =
426 5.443, p =0.0077). (F) Dendritic field (mm^2) (ANOVA (F2, 44) = 0.8512, p=0.4338). (G) Sholl
427 profiles.

428

429 **Methods**

430

431 ***Drosophila* stocks and genetics:** Fly stocks were obtained from the Bloomington
432 Drosophila Stock Centre ($spir^{1}$, $spir^{2F}$, $spir^{DfExel6046}$ (referred to as $spir^{Df}$), Mi05646, Mi05737,
433 *UAS-capu::GFP*, w^{1118}, *UAS-mCD8::GFP*, *UAS-Rab11::GFP*, *UAS-Rab4::mRFP*, *UAS-*
434 *Rab6::GFP*, *UAS-Rab11-dsRNA*, *UAS-LifeAct-GFP*. *ppk-GAL4* and *ppkCD4::tdTom* were
435 gifts from Dr. Yuh-Nung Jan. *UAS-Rab11::mCherry* was a gift from Dr. Gregory Emery. *nSyb-*
436 *GAL4* line was created by Dr Julie Simpson, for which we used 2nd chromosome insertions
437 generated by Dr Stefan Thor. To create the lines *UAS-spir::GFP*, *UAS-spir::tdTom*, *UAS-*
438 $spir^{Y232K}$*::GFP*, *UAS-*$spir^{ABCD}$*::GFP*, *UAS-*$spir^{\Delta SB}$*::GFP*, *UAS-*$spir^{C5,6S}$*::GFP*, DNA
439 constructs encoding full-length Spir or each of the 4 mutated versions (Kerkhoff *et al.*, 2001;

440 Quinlan, 2013; Quinlan *et al.*, 2005) were designed to add C-terminal GFP or tdTomato
441 (tdTom) fluorophores. These constructs were subcloned into the vector pMUH, then
442 microinjected by standard procedures (Bestgene, Inc) to target the VK00027 landing site in the
443 *Drosophila* genome with φc31-mediated transposition (Pfeiffer et al., 2010). $spir^{GAL4}$ was
444 generated by inserting a so-called Trojan-GAL4 into the *spir* locus (Diao et al., 2015; Venken
445 et al., 2011). pT-GEM(0) a gift from Benjamin White (Addgene plasmid # 62891) was
446 microinjected (Bestgene, Inc) into MiMIC line, Mi05646 (Diao *et al.*, 2015; Venken *et al.*,
447 2011). The same plasmid was injected into MiMIC line Mi05737 to generate $capu^{GAL4}$.

448 **Antibodies:** To produce anti-Spir antisera, DNA encoding Spir amino acids 565-692
449 were cloned into pGEX-6P-1 to produce an IPTG-inducible C-terminal GST fusion proteins in
450 BL21 cells. The purified GST fusion protein was injected into two rabbits and the serum was
451 extracted according to approved protocols at the Comparative Medicine and Animal
452 Resources Centre (McGill University) and standards established by the Canadian Council on
453 Animal Care. Crude serum (500 µl) was then pre-absorbed by overnight incubation with 500
454 µl L3 larvae ($spir^{1}/spir^{Df}$) that had been fixed previously in 4% PFA. Another primary antibody
455 for IHC was Alexa-647-conjugated goat anti-HRP (1:800, Jackson ImmunoResearch
456 #123605021), while secondary antibody for anti Spir IHC was Alexa-647-conjugated goat anti-
457 rabbit (1:1000, Invitrogen, #A21244). For western blotting, membranes were incubated with
458 mouse anti-GFP (Clontech #632380), rabbit anti-DsRed (Takara #632496), mouse anti-Actin
459 (Sigma #A4700) or rabbit anti-Spire (directed at amino acids 565-692). For detection, HRP-
460 conjugated secondary antibodies (anti-mouse and anti-rabbit (both 1:3000, BioRad) were used
461 and revealed with chemiluminescence (Amersham ECL Western Blotting Detection Reagents).

462 **Immunohistochemistry (IHC):** Third instar larvae (L3) of either sex were dissected
463 in Sorensen phosphate buffer (pH 7.4) and fixed in 4% paraformaldehyde (in Sorensen's
464 buffer) for 10 minutes (min) at room temperature. Washes (3X over 20 min) were done with

465 Sorensen's buffer containing 0.2% Triton-X-100 (Sigma). Specimens were then blocked with
466 Sorensen's buffer containing 5% normal goat serum (NGS), incubated at 4°C with primary
467 antibodies overnight, washed as above, then incubated with secondary antibodies for 2 hours
468 at room temperature. Anti-Spir antiserum for immunohistochemistry was directed at amino
469 acids 1-91. Primary and secondary antibodies were diluted in Sorensen's buffer containing 5%
470 NGS. After a final wash as above, specimens were then mounted with SlowFade Diamond
471 Antifade Mountant (Invitrogen) for imaging.

472 **Co-immunoprecipitation (co-IP) and western blotting:** Lysates for co-IPs and
473 western blots were made from adult heads aged 1-5 days after eclosion. For western blots,
474 heads were mechanically crushed using a motorized pestle directly in 2X Laemmli buffer. For
475 co-IPs, 100 heads were cut and collected on dry ice, then mechanically crushed using a
476 motorized pestle in 100ul of lysis buffer containing 50mM Tris pH, 150mM KCl, 1mM MgCl2,
477 1mM EGTA, Roche protease inhibitor cocktail and 10% glycerol. Lysates were treated with
478 10% deoxycholic acid and 10% Triton X-100, then incubated overnight on a Nutator with anti-
479 GFP bound agarose beads (Chromotek GFP-Trap® #gta). Lysates and beads were separated in
480 a centrifuge, washed with a glycerol free buffer, and the complexes on the beads were
481 dissociated directly in Laemmli buffer, then separated using standard SDS-PAGE and wet-
482 transfer procedures.

483 **Imaging:** All imaging and quantification was of ddaC, the dorsal-most c4da neuron,
484 in abdominal segments of the larval body wall. For static images, third instar (L3) larvae were
485 dissected and prepared for IHC, or they were squished directly on the slide in 100% glycerol
486 and prepared for imaging of native fluorescence (GFP, tdTom, mCherry, mRFP) within 10
487 minutes. Static images were taken with an Olympus Fluoview FV-1000/BX63 confocal
488 microscope using either a 20X or 60X oil-immersion objective lens. All time-lapse imaging
489 was done on L2 larvae, where eggs were initially collected for 4h on agar plates containing

490 grape juice and yeast. After 24h, hatched larvae of selected genotypes were transferred on a
491 fresh fly food plate to start timing. L2 larvae (65h ± 4h AEL) were mounted in a drop of
492 halocarbon oil in a polydimethylsiloxane (PDMS) microfluid device, and then imaged by live
493 confocal microscopy (Zeiss, Spinning Disk, Inverted Axio Observer Z1) with 63x objective
494 lens, at room temperature with Immersol W (Zeiss) between lens and coverslip. Using Zen
495 software (Zeiss), live imaging of fluorescent proteins GFP and tdTomato was performed for 5
496 min with 5s interval on average. If GFP only, then the interval was 2s on average. Only videos
497 obtained from larvae that were still alive and active after imaging were used for analysis. Each
498 video was then registered on ImageJ using StackReg plugin (Thevenaz et al., 1998) before
499 analysis.

500 **Quantification of Lifeact::GFP and Spir::GFP localization:** New branches
501 appearing in each movie were identified, and initiation sites were classified as having "de
502 novo" actin polymer if a punctum of LifeAct::GFP intensity appeared at the site and grew in
503 intensity until protrusion of the new branch. Initiation sites had "pre-formed" actin if motile
504 blobs of LifeAct::GFP were observed to arrive prior to branch outgrowth (motile). New
505 branches for which a LifeAct::GFP punctum was at the initiation site in the first frame of the
506 movie were not considered because it was uncertain when or how this actin arose there.
507 Consistent with a previous report (Nithianandam and Chien, 2018), we observed only a single
508 rare instance where a filopodium grew from an initiation site where LifeAct::GFP was not
509 detected.

510 To measure the association of Spir::GFP labeled punctae to either a dendrite shaft,
511 branch point, or tip, a custom routine was developed to extract this information from images
512 acquired with a 20X objective (2 to 4 images stitched together where necessary using the
513 Pairwise Stitching plugin (Preibisch et al., 2009). From maximum intensity projections (MIP)
514 of 10 c4da neurons (ddaC) labeled for the dendrite marker CD4-tdTom, signal from beyond

515 the cell of interest was cleared manually, the background was subtracted, and a MIP mask
516 created. This mask was then applied to the SpirFL:: GFP channel. Pixels outside the mask was
517 cleared. The MIP mask was skeletonized using Fiji's skeletonization plugin (Arganda-Carreras
518 et al., 2010) to obtain the location of shafts, branch points, and tips. A script from the
519 Neuroantomy update site was then used to determine which Spir::GFP punctae were associated
520 with such skeleton features. When a Spir::GFP punctum was 3 µm or less (snap-to distance)
521 from either a branch point or tip it was assigned to each, respectively. This snap-to distance
522 was selected because from a representative Spir:GFP image, 80% of the punctae had a diameter
523 of 3 µm or less. Additionally, no branch points or tips were 3 µm or less apart from one another.
524 The number of punctae at branch points and tips was then divided by the total number of branch
525 points and tips, respectively, to obtain the percent of branch points and tips that were occupied
526 by Spir::GFP.

527 **Dendrite morphometry**: c4da neurons (ddaC) were imaged at 20X, with 1 image field
528 usually sufficient to capture the entire dendritic field of a neuron. However, in some cases 2
529 images were stitched together using the Fiji plugin Pairwise Stitching to generate an image of
530 the entire neuron (Preibisch *et al.*, 2009). Maximum intensity projections of confocal z-series
531 image stacks were segmented as described previously (Ferreira *et al.*, 2014a). Various Fiji
532 plugins were used to determine branching characteristics of neurons; Sholl Analysis to generate
533 Sholl profiles and extract Sholl related parameters (Ferreira *et al.*, 2014b), Strahler Analysis to
534 assess the number of terminal dendrites (Ferreira *et al.*, 2014b; Strahler, 1957), and Analyze
535 Skeleton for total arbor length. Dendritic field was determined by fitting a polygon around the
536 segmented neuron on Fiji, and measuring the area inside the shape (Schindelin et al., 2012).

537 **Measuring dendrite dynamics:** Pre-existing dendrites at the beginning of live imaging
538 movies were analyzed for the dynamics of their terminal branches using MTrackJ (Meijering
539 et al., 2012). Terminal branch length was compared by an observer every frame (every 5s on

540 average) for the entire duration (5 min) of each movie. Dendrites that extended, retracted, or
541 did both, or remained static were recorded, and these numbers were expressed as the percentage
542 of the total number of pre-existing dendrites at the beginning of each movie. Newly formed
543 dendrites were tracked in a similar manner (every 5s), and their numbers expressed as a
544 percentage of the total number of terminal branches seen at the beginning of each movie. To
545 measure their protrusive characteristics during outgrowth, mean speed was the average of the
546 speeds of growth for each frame (including extensions and pauses) until the branch stopped
547 growing altogether, or retracted, or the movie ended. The proportion of time the branch spent
548 paused during this period of saltatory outgrowth was calculated, as was the maximum length
549 of its protrusion.

550 **Graphs and Statistics:** Bar graphs and statistics were done using GraphPad Prism v9,
551 and displayed data is expressed as mean ± standard error. For comparisons of more than two
552 conditions, data were tested for normal distribution using D'Agostino & Pearson test and
553 analysed for statistical significance using one-way ANOVA (multiple groups). Following
554 ANOVA at $P<0.05$, Dunnett's post-hoc tests were performed. For the repeated measures of
555 western blots, Friedman test was applied then Dunn's post-hoc tests. To compare two
556 conditions, Student's t-test was used. Asterisks indicate the significance of *P*-values compared
557 to the indicated control group (*P<0.05, **P<0.01, ***P<0.001, ****P<0.0001).

558

559 **Supplemental Information**

560 **Supplemental Figure S1: Spir expression and motility in dendrites** (related to Figure 1).
561 (A) Co-labeling for endogenous Spir and horseradish peroxidase (HRP) in the body wall of an
562 L3 larva, using IHC. Spir expression observed in a c4da neuron (arrowhead, left panel) in a
563 $spir^{1}/+$ heterozygote, but not in a $spir^{1/Df}$ hemizygous mutant (arrowhead, right panel). (B)
564 Anti-Spir western blot of lysates from dissected adult brains, comparing controls with $spir^{1/Df}$

565 mutants and with flies overexpressing Spir::GFP in all neurons with nSyb-Gal4. Expected mass
566 of Spir::GFP is 142kDa, while that of Spir is 115kDa. The increased presence of Spir (115
567 kDa) upon overexpression of Spir::GFP likely arises from proteolytic cleavage of the GFP tag
568 from Spir::GFP fusion protein. (C) ppk-Gal4 driven Spir::GFP expression is detected strongly
569 with anti-Spir IHC in a c4da neuron cell soma (white arrowhead) and in puncta within at
570 dendrite branch points (e.g., orange arrowhead), and dendrite shafts (e.g., blue arrowhead)
571 Scale bars (A, B) = 50um. (D) High magnification view of Spir::GFP (native GFP, green) in
572 c4da neuron dendrites (tdTom, magenta) of an L3 larva. Based on size, morphology and
573 location, the types of Spir::GFP-positive puncta in dendrites include large, irregularly shaped
574 puncta at branch points (e.g., orange arrowhead), and smaller, circular puncta in dendrite shafts
575 (e.g., blue arrowhead) or at branch tips (e.g., yellow arrowhead). (E) Locations of Spir::GFP
576 puncta observed in static images of c4da dendrite arbors at L3 (n=10 neurons). (F) Greyscale
577 filmstrip (Supplemental Video 4, acquired at ~1 frame/2s) from a c4da neuron of an L2 larva,
578 where the black arrowhead indicates progressive movement of a Spir::GFP-labelled punctum
579 within a dendrite shaft. Scale bar: 5μm. Motile Spir::GFP puncta moved in both anterograde
580 (64%) and retrograde (36%) directions from the cell soma, and sometimes were observed to
581 switch from to the other. Some puncta appeared to pass one another, while others merged.
582 Motile Spir::GFP particles were found to travel 0.6 um/s on average, and achieved a maximal
583 speed of 1.1 um/s.
584

585 **Supplemental Figure S2: Quantification of dynamics of terminal branches that pre-**
586 **existed at onset of time-lapse movies** (related to Figure 2). (A-D) Quantification of percentage
587 of branches that extended (A, ANOVA ($F(3, 39) = 0.1262$, $p = 0.9440$), retracted (B, ANOVA
588 ($F(3, 39) = 0.8598$, $p = 0.47$), extended and retracted in the same movie (C, ANOVA ($F(3, 39)$
589 $= 2.348$, $p = 0.0875$) or remained static (D, ANOVA ($F(3, 39) = 1.983$, $p = 0.1324$). Graphs

590 show mean±SEM. (E-G) Protrusive growth characteristics of nascent branches in controls (+/+,
591 n=14) and *spir* mutants ($spir^{2F}/spir^{Df}$, n=7) in L2 larvae expressing LifeAct::GFP driven by
592 *ppk-GAL4*, including mean speed (E, t-test (t(21) = 1,757, p = 0,0951), time paused (F, t-
593 test(t(21) = 0,7025, p = 0,4909), and maximum protrusion length (G, t-test (t(21) = 1,516, p =
594 0,1459). Graphs show scatter plot for each branch, with mean ± SEM indicated (ns, not
595 significant).
596
597 **Supplemental Figure S3: Quantification of dynamics of newly formed and pre-existing**
598 **terminal branches** (related to Figure 2). (A-B) Dendrite parameters from time-lapse movies
599 of c4da neurons (labeled with ppkCD4::tdTom) in L2 larvae expressing LifeAct::GFP driven
600 by *ppk-GAL4*. Graphs show mean ± SEM, comparing controls (+/+, n=11) with *spir*
601 heterozygotes ($spir^{2F}$/+, n=8) and *spir* mutants ($spir^{2F}/spir^{Df}$, n=11). Asterisks indicate
602 significant changes compared to +/+ heterozygous controls (*P<0.05). (A) Number of terminal
603 branches per μm^2 of area in first frame of each movie. (ANOVA (F(2, 27) = 4.079, p = 0.0283).
604 (B) Proportion of new/total branches in each movie (ANOVA (F(2, 27) = 3.376, p = 0.0491).
605 (C-F) For branches that pre-existed in the first frame of each movie, quantification of
606 percentage of the number of branches that extended (C, ANOVA (F(2, 27) = 0.0129, p =
607 0.9872), retracted (D, ANOVA (F(2, 27) = 0.7537, p = 0.4803), extended and retracted in the
608 same movie (E, ANOVA (F(2, 27) = 1.979, p = 0.1577) or remained static (F, ANOVA (F(2,
609 27) = 0.05392, p = 0.9476).
610
611 **Supplemental Figure S4: Dendrite parameters for c4da neurons in L3 larvae** (related to
612 Figure 2). (A-D) This is the same dataset shown in Fig. 2, except it was adjusted to control for
613 dendritic field size by removing from the analysis four $spir^{2F/Df}$ c4da neurons with unusually
614 small arbors (n=11). Graphs show mean ± SEM). Asterisks indicate significant changes

615 compared to *spir*^{2F}/+ heterozygous controls. (A) Dendritic field per ddaC neuron (mm^2)
616 (ANOVA ($F(4, 66) = 1.912$, $p = 0.1189$. (B) Total number of terminal dendrites per ddaC
617 neuron (ANOVA ($F(4, 66) = 9.328$, $p < 0.0001$). (C) Total length of dendrite arbor per ddaC
618 neuron (mm) (ANOVA ($F(4,66) = 12.03$, $p < 0.0001$). (D) Sholl critical value (ANOVA ($F(4,$
619 $66) = 6.914$, $p = 0.0001$).

620

621 **Supplemental Figure S5: Function, expression, and distribution of Spir::GFP bearing**
622 **domain-specific mutations** (related to Figure 3). (A) Sholl profiles for entire ddaC neurons
623 labelled with ppk-CD4::tdTom. (B) Anti-GFP western blot from adult heads of animals
624 overexpressing in all neurons either intact Spir::GFP or Spir::GFP bearing domain-specific
625 mutations. One of three replicate blots, this blot is distinct from the one shown in Fig. 3C and
626 is shown in its entirety. The expected molecular weight of Spir::GFP is 142 kDa, and that of
627 GFP is 27 kDa, and so proteolytic cleavage of GFP is not apparent for most constructs. (C)
628 *ppk-GAL4* drives the expression of Spir^{Y232K}::GFP or Spir^{ABCD}::GFP or Spir^{C5,6S}::GFP in a *spir*
629 mutant background. Punctate distribution of Spir::GFP is maintained for each of these
630 mutations. White boxes in left panels indicate areas magnified in panels to their right. Scale
631 bar=50μm.

632

633 **Supplemental Figure S6: Expression, and distribution of Spir::GFP bearing domain-**
634 **specific mutations** (related to Figure 4). (A) *ppk-GAL4*-driven expression of Spir::GFP and
635 Rab4::mRFP. Cell bodies of ddaC neurons are indicated (white arrowheads). Co-localization
636 of Spir::GFP with Rab4:mRFP is observed at branch points (e.g., orange arrowhead) and
637 dendrite shafts (e.g., blue arrowhead). (B, C) Distribution of Spir::GFP in c4da neurons in
638 controls (B) and upon expression Rab11-dsRNAi in c4da neurons with *ppk-Gal4* (C). White

639 boxes in left panels indicate areas magnified in panels to their right. Punctate distribution of
640 Spir::GFP within dendrite arbors of c4da neurons was seemingly unaffected by the knockdown
641 of Rab11. Scale bars=50µm.

642

643 **Supplemental Video 1 – corresponding to Fig. 1A**

644 **Supplemental Video 2 - corresponding to Fig. 1B**

645 **Supplemental Video 3 - corresponding to Fig. 1E**

646 **Supplemental Video 4 - corresponding to Supplemental Fig. S1F**

647 **Supplemental Video 5 - corresponding to Fig. 1H**

648 **Supplemental Video 6 - corresponding to Fig. 1I**

649

650 **References**

651 Alzahofi, N., Welz, T., Robinson, C.L., Page, E.L., Briggs, D.A., Stainthorp, A.K., Reekes, J.,
652 Elbe, D.A., Straub, F., Kallemeijn, W.W., et al. (2020). Rab27a co-ordinates actin-dependent
653 transport by controlling organelle-associated motors and track assembly proteins. Nat Commun
654 *11*, 3495. 10.1038/s41467-020-17212-6.

655 Andersen, R., Li, Y., Resseguie, M., and Brenman, J.E. (2005). Calcium/calmodulin-dependent
656 protein kinase II alters structural plasticity and cytoskeletal dynamics in Drosophila. J Neurosci
657 *25*, 8878-8888. 25/39/8878 [pii]

658 10.1523/JNEUROSCI.2005-05.2005.

659 Arganda-Carreras, I., Fernandez-Gonzalez, R., Munoz-Barrutia, A., and Ortiz-De-Solorzano,
660 C. (2010). 3D reconstruction of histological sections: Application to mammary gland tissue.
661 Microsc Res Tech *73*, 1019-1029. 10.1002/jemt.20829.
662 Das, R., Bhattacharjee, S., Letcher, J.M., Harris, J.M., Nanda, S., Foldi, I., Lottes, E.N., Bobo,
663 H.M., Grantier, B.D., Mihaly, J., et al. (2021). Formin 3 directs dendritic architecture via
664 microtubule regulation and is required for somatosensory nociceptive behavior. Development
665 *148*. 10.1242/dev.187609.
666 Diao, F., Ironfield, H., Luan, H., Diao, F., Shropshire, W.C., Ewer, J., Marr, E., Potter, C.J.,
667 Landgraf, M., and White, B.H. (2015). Plug-and-play genetic access to drosophila cell types
668 using exchangeable exon cassettes. Cell reports *10*, 1410-1421. 10.1016/j.celrep.2015.01.059.
669 Eva, R., Dassie, E., Caswell, P.T., Dick, G., ffrench-Constant, C., Norman, J.C., and Fawcett,
670 J.W. (2010). Rab11 and its effector Rab coupling protein contribute to the trafficking of beta 1
671 integrins during axon growth in adult dorsal root ganglion neurons and PC12 cells. J Neurosci
672 *30*, 11654-11669. 10.1523/JNEUROSCI.2425-10.2010.
673 Ferreira, T., Ou, Y., Li, S., Giniger, E., and van Meyel, D.J. (2014a). Dendrite architecture
674 organized by transcriptional control of the F-actin nucleator Spire. Development *141*, 650-660.
675 10.1242/dev.099655.
676 Ferreira, T.A., Blackman, A.V., Oyrer, J., Jayabal, S., Chung, A.J., Watt, A.J., Sjostrom, P.J.,
677 and van Meyel, D.J. (2014b). Neuronal morphometry directly from bitmap images. Nat
678 Methods *11*, 982-984. 10.1038/nmeth.3125.
679 Grueber, W.B., Jan, L.Y., and Jan, Y.N. (2002). Tiling of the Drosophila epidermis by
680 multidendritic sensory neurons. Development *129*, 2867-2878.
681 Grueber, W.B., Yang, C.H., Ye, B., and Jan, Y.N. (2005). The development of neuronal
682 morphology in insects. Curr Biol *15*, R730-738.

683 Holubcova, Z., Howard, G., and Schuh, M. (2013). Vesicles modulate an actin network for
684 asymmetric spindle positioning. Nature cell biology *15*, 937-947. 10.1038/ncb2802.
685 Hou, W., Izadi, M., Nemitz, S., Haag, N., Kessels, M.M., and Qualmann, B. (2015). The Actin
686 Nucleator Cobl Is Controlled by Calcium and Calmodulin. PLoS Biol *13*, e1002233.
687 10.1371/journal.pbio.1002233.
688 Kennedy, M.J., and Hanus, C. (2019). Architecture and Dynamics of the Neuronal Secretory
689 Network. Annual review of cell and developmental biology *35*, 543-566. 10.1146/annurev-
690 cellbio-100818-125418.
691 Kerkhoff, E., Simpson, J.C., Leberfinger, C.B., Otto, I.M., Doerks, T., Bork, P., Rapp, U.R.,
692 Raabe, T., and Pepperkok, R. (2001). The Spir actin organizers are involved in vesicle transport
693 processes. Curr Biol *11*, 1963-1968. S0960-9822(01)00602-9 [pii].
694 Kiral, F.R., Kohrs, F.E., Jin, E.J., and Hiesinger, P.R. (2018). Rab GTPases and Membrane
695 Trafficking in Neurodegeneration. Curr Biol *28*, R471-R486. 10.1016/j.cub.2018.02.010.
696 Konietzny, A., Bar, J., and Mikhaylova, M. (2017). Dendritic Actin Cytoskeleton: Structure,
697 Functions, and Regulations. Frontiers in cellular neuroscience *11*, 147.
698 10.3389/fncel.2017.00147.
699 Korobova, F., and Svitkina, T. (2010). Molecular architecture of synaptic actin cytoskeleton in
700 hippocampal neurons reveals a mechanism of dendritic spine morphogenesis. Mol Biol Cell
701 *21*, 165-176. E09-07-0596 [pii]
702 10.1091/mbc.E09-07-0596.
703 Kramer, R., Rode, S., and Rumpf, S. (2019). Rab11 is required for neurite pruning and
704 developmental membrane protein degradation in Drosophila sensory neurons. Dev Biol *451*,
705 68-78. 10.1016/j.ydbio.2019.03.003.
706 Lanoue, V., and Cooper, H.M. (2019). Branching mechanisms shaping dendrite architecture.
707 Dev Biol *451*, 16-24. 10.1016/j.ydbio.2018.12.005.

708 Lasiecka, Z.M., and Winckler, B. (2011). Mechanisms of polarized membrane trafficking in
709 neurons -- focusing in on endosomes. Mol Cell Neurosci *48*, 278-287.
710 10.1016/j.mcn.2011.06.013.
711 Lefebvre, J.L. (2021). Molecular mechanisms that mediate dendrite morphogenesis. Curr Top
712 Dev Biol *142*, 233-282. 10.1016/bs.ctdb.2020.12.008.
713 Lefebvre, J.L., Sanes, J.R., and Kay, J.N. (2015). Development of dendritic form and function.
714 Annual review of cell and developmental biology *31*, 741-777. 10.1146/annurev-cellbio-
715 100913-013020.
716 London, M., and Hausser, M. (2005). Dendritic computation. Annual review of neuroscience
717 *28*, 503-532.
718 Luo, L. (2021). Architectures of neuronal circuits. Science *373*, eabg7285.
719 10.1126/science.abg7285.
720 Manor, U., Bartholomew, S., Golani, G., Christenson, E., Kozlov, M., Higgs, H., Spudich, J.,
721 and Lippincott-Schwartz, J. (2015). A mitochondria-anchored isoform of the actin-nucleating
722 spire protein regulates mitochondrial division. Elife *4*. 10.7554/eLife.08828.
723 Manseau, L.J., and Schupbach, T. (1989). cappuccino and spire: two unique maternal-effect
724 loci required for both the anteroposterior and dorsoventral patterns of the Drosophila embryo.
725 Genes & development *3*, 1437-1452.
726 Marat, A.L., and Haucke, V. (2016). Phosphatidylinositol 3-phosphates-at the interface
727 between cell signalling and membrane traffic. The EMBO journal *35*, 561-579.
728 10.15252/embj.201593564.
729 Medina, P.M., Swick, L.L., Andersen, R., Blalock, Z., and Brenman, J.E. (2006). A novel
730 forward genetic screen for identifying mutations affecting larval neuronal dendrite
731 development in Drosophila melanogaster. Genetics *172*, 2325-2335.

732 Meijering, E., Dzyubachyk, O., and Smal, I. (2012). Methods for cell and particle tracking.
733 Methods Enzymol *504*, 183-200. 10.1016/B978-0-12-391857-4.00009-4.
734 Nagel, A.C., Apidianakis, Y., Wech, I., Maier, D., Delidakis, C., and Preiss, A. (2000). Neural
735 hyperplasia induced by RNA interference with m4/malpha gene activity. Mechanisms of
736 development *98*, 19-28.
737 Nithianandam, V., and Chien, C.T. (2018). Actin blobs prefigure dendrite branching sites. The
738 Journal of cell biology *217*, 3731-3746. 10.1083/jcb.201711136.
739 Pai, Y.J., and Moore, A.W. (2018). Dendritic actin delivery service. The Journal of cell biology
740 *217*, 3325-3326. 10.1083/jcb.201808095.
741 Park, M., Penick, E.C., Edwards, J.G., Kauer, J.A., and Ehlers, M.D. (2004). Recycling
742 endosomes supply AMPA receptors for LTP. Science *305*, 1972-1975.
743 10.1126/science.1102026

744 305/5692/1972 [pii].
745 Pfeiffer, B.D., Ngo, T.T., Hibbard, K.L., Murphy, C., Jenett, A., Truman, J.W., and Rubin,
746 G.M. (2010). Refinement of tools for targeted gene expression in Drosophila. Genetics *186*,
747 735-755. 10.1534/genetics.110.119917.
748 Pfender, S., Kuznetsov, V., Pleiser, S., Kerkhoff, E., and Schuh, M. (2011). Spire-type actin
749 nucleators cooperate with Formin-2 to drive asymmetric oocyte division. Curr Biol *21*, 955-
750 960. S0960-9822(11)00468-4 [pii]

751 10.1016/j.cub.2011.04.029.
752 Pleiser, S., Rock, R., Wellmann, J., Gessler, M., and Kerkhoff, E. (2010). Expression patterns
753 of the mouse Spir-2 actin nucleator. Gene expression patterns : GEP *10*, 345-350. S1567-
754 133X(10)00080-3 [pii]

755 10.1016/j.gep.2010.08.001.

Preibisch, S., Saalfeld, S., and Tomancak, P. (2009). Globally optimal stitching of tiled 3D microscopic image acquisitions. Bioinformatics *25*, 1463-1465. btp184 [pii]

10.1093/bioinformatics/btp184.

Pylypenko, O., Welz, T., Tittel, J., Kollmar, M., Chardon, F., Malherbe, G., Weiss, S., Michel, C.I., Samol-Wolf, A., Grasskamp, A.T., et al. (2016). Coordinated recruitment of Spir actin nucleators and myosin V motors to Rab11 vesicle membranes. Elife *5*. 10.7554/eLife.17523.

Quinlan, M.E. (2013). Direct interaction between two actin nucleators is required in Drosophila oogenesis. Development *140*, 4417-4425. 10.1242/dev.097337.

Quinlan, M.E., Heuser, J.E., Kerkhoff, E., and Mullins, R.D. (2005). Drosophila Spire is an actin nucleation factor. Nature *433*, 382-388. nature03241 [pii]

10.1038/nature03241.

Quinlan, M.E., Hilgert, S., Bedrossian, A., Mullins, R.D., and Kerkhoff, E. (2007). Regulatory interactions between two actin nucleators, Spire and Cappuccino. The Journal of cell biology *179*, 117-128. jcb.200706196 [pii]

10.1083/jcb.200706196.

Rottner, K., Faix, J., Bogdan, S., Linder, S., and Kerkhoff, E. (2017). Actin assembly mechanisms at a glance. J Cell Sci *130*, 3427-3435. 10.1242/jcs.206433.

Schindelin, J., Arganda-Carreras, I., Frise, E., Kaynig, V., Longair, M., Pietzsch, T., Preibisch, S., Rueden, C., Saalfeld, S., Schmid, B., et al. (2012). Fiji: an open-source platform for biological-image analysis. Nat Methods *9*, 676-682. 10.1038/nmeth.2019

nmeth.2019 [pii].

Schuh, M. (2011). An actin-dependent mechanism for long-range vesicle transport. Nature cell biology *13*, 1431-1436. 10.1038/ncb2353

ncb2353 [pii].

780 Schumacher, N., Borawski, J.M., Leberfinger, C.B., Gessler, M., and Kerkhoff, E. (2004).
781 Overlapping expression pattern of the actin organizers Spir-1 and formin-2 in the developing
782 mouse nervous system and the adult brain. Gene expression patterns : GEP *4*, 249-255.
783 10.1016/j.modgep.2003.11.006

784 S1567133X03002096 [pii].

785 Shi, R., Kramer, D.A., Chen, B., and Shen, K. (2021). A two-step actin polymerization
786 mechanism drives dendrite branching. Neural Dev *16*, 3. 10.1186/s13064-021-00154-0.

787 Sholl, D.A. (1953). Dendritic organization in the neurons of the visual and motor cortices of
788 the cat. Journal of anatomy *87*, 387-406.

789 Siton-Mendelson, O., and Bernheim-Groswasser, A. (2017). Functional Actin Networks under
790 Construction: The Cooperative Action of Actin Nucleation and Elongation Factors. Trends
791 Biochem Sci *42*, 414-430. 10.1016/j.tibs.2017.03.002.

792 Sonnichsen, B., De Renzis, S., Nielsen, E., Rietdorf, J., and Zerial, M. (2000). Distinct
793 membrane domains on endosomes in the recycling pathway visualized by multicolor imaging
794 of Rab4, Rab5, and Rab11. The Journal of cell biology *149*, 901-914.

795 Strahler, A.N. (1957). Quantitative analysis of watershed geomorphology. Transactions of the
796 American Geophysical Union *38*, 913-920.

797 Sturner, T., Ferreira Castro, A., Philipps, M., Cuntz, H., and Tavosanis, G. (2022). The
798 branching code: A model of actin-driven dendrite arborization. Cell reports *39*, 110746.
799 10.1016/j.celrep.2022.110746.

800 Sturner, T., Tatarnikova, A., Mueller, J., Schaffran, B., Cuntz, H., Zhang, Y., Nemethova, M.,
801 Bogdan, S., Small, V., and Tavosanis, G. (2019). Transient localization of the Arp2/3 complex
802 initiates neuronal dendrite branching in vivo. Development *146*. 10.1242/dev.171397.

803 Thevenaz, P., Ruttimann, U.E., and Unser, M. (1998). A pyramid approach to subpixel
804 registration based on intensity. IEEE Trans Image Process *7*, 27-41. 10.1109/83.650848.

805 Tittel, J., Welz, T., Czogalla, A., Dietrich, S., Samol-Wolf, A., Schulte, M., Schwille, P.,
806 Weidemann, T., and Kerkhoff, E. (2015). Membrane targeting of the Spir.formin actin
807 nucleator complex requires a sequential handshake of polar interactions. The Journal of
808 biological chemistry *290*, 6428-6444. 10.1074/jbc.M114.602672.
809 Venken, K.J., Schulze, K.L., Haelterman, N.A., Pan, H., He, Y., Evans-Holm, M., Carlson,
810 J.W., Levis, R.W., Spradling, A.C., Hoskins, R.A., and Bellen, H.J. (2011). MiMIC: a highly
811 versatile transposon insertion resource for engineering Drosophila melanogaster genes. Nat
812 Methods *8*, 737-743.
813 Vizcarra, C.L., Kreutz, B., Rodal, A.A., Toms, A.V., Lu, J., Zheng, W., Quinlan, M.E., and
814 Eck, M.J. (2011). Structure and function of the interacting domains of Spire and Fmn-family
815 formins. Proc Natl Acad Sci U S A *108*, 11884-11889. 1105703108 [pii]
816 10.1073/pnas.1105703108.
817 Wellington, A., Emmons, S., James, B., Calley, J., Grover, M., Tolias, P., and Manseau, L.
818 (1999). Spire contains actin binding domains and is related to ascidian posterior end mark-5.
819 Development *126*, 5267-5274.
820 Willig, K.I., Steffens, H., Gregor, C., Herholt, A., Rossner, M.J., and Hell, S.W. (2014).
821 Nanoscopy of filamentous actin in cortical dendrites of a living mouse. Biophys J *106*, L01-
822 03. 10.1016/j.bpj.2013.11.1119.
823 Yoong, L.F., Lim, H.K., Tran, H., Lackner, S., Zheng, Z., Hong, P., and Moore, A.W. (2020).
824 Atypical Myosin Tunes Dendrite Arbor Subdivision. Neuron *106*, 452-467 e458.
825 10.1016/j.neuron.2020.02.002.
826 Zou, W., Dong, X., Broederdorf, T.R., Shen, A., Kramer, D.A., Shi, R., Liang, X., Miller,
827 D.M., 3rd, Xiang, Y.K., Yasuda, R., et al. (2018). A Dendritic Guidance Receptor Complex
828 Brings Together Distinct Actin Regulators to Drive Efficient F-Actin Assembly and Branching.
829 Developmental cell *45*, 362-375 e363. 10.1016/j.devcel.2018.04.008.

Figure 1

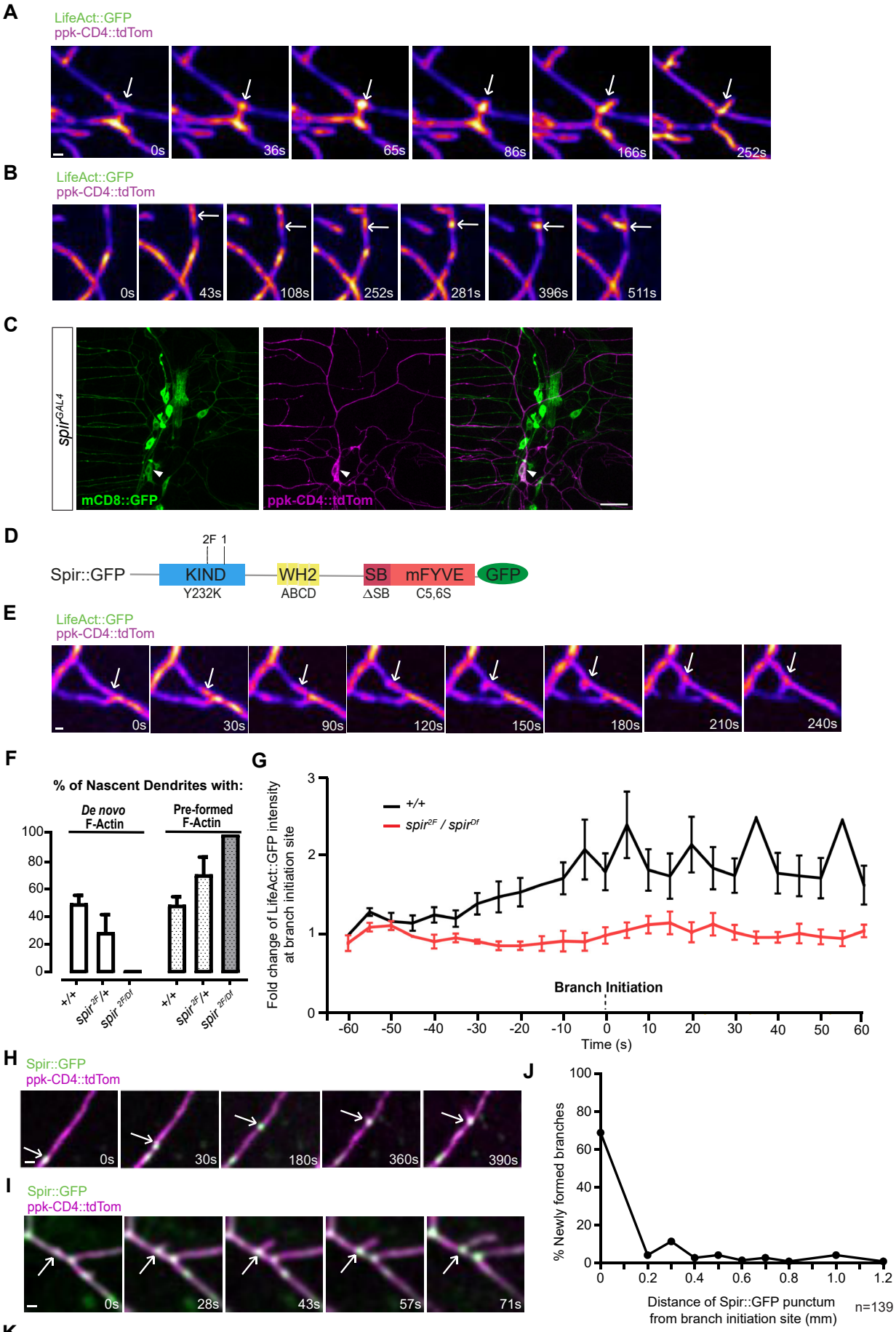

K

Spir::GFP puncta at branch initiation sites in time-lapse movies at L2 (n=61)				
	Occurrence	Time (s) from stationary punctum to branch outgrowth		
		Minimum	Maximum	Mean ±sd
Spir::GFP observed to move to site	30%	4	129	43 ± 41
Spir::GFP stationed at site in first movie frame	70%	8	229	88 ± 67

Figure 2

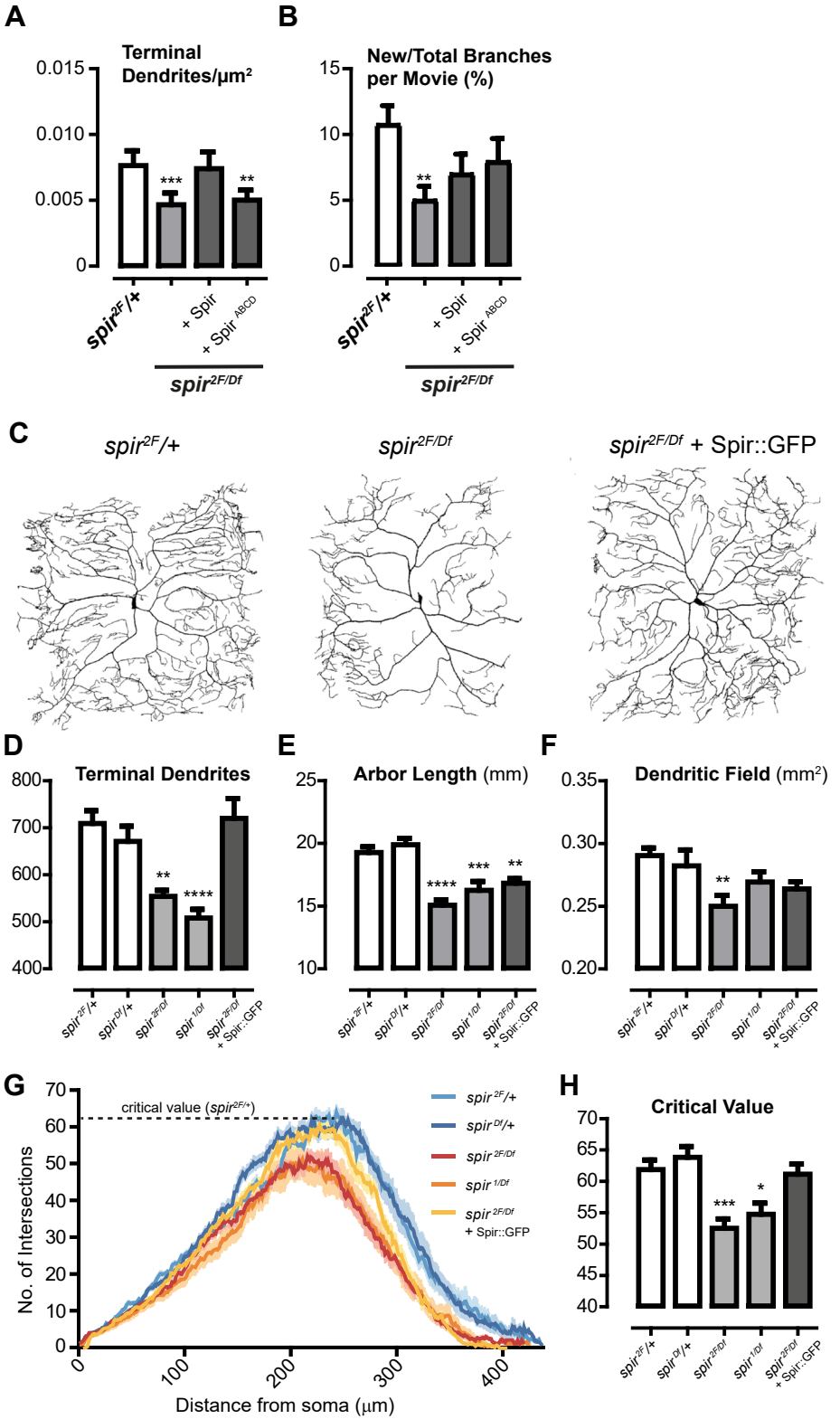
A
Terminal Dendrites/µm²
0.015
0.010
0.005
0
***
**
spir2F/+
+ Spir
+ Spir ABCD
spir2F/Df
B
New/Total Branches per Movie (%)
15
10
5
0
**
spir2F/+
+ Spir
+ Spir ABCD
spir2F/Df
C
spir2F/+
spir2F/Df
spir2F/Df + Spir::GFP
D
Terminal Dendrites
800
700
600
500
400
**
****
spir2F/+
spirDf/+
spir2F/Df
spir1/Df
spir2F/Df + Spir::GFP
E
Arbor Length (mm)
25
20
15
10
****
***
**
spir2F/+
spirDf/+
spir2F/Df
spir1/Df
spir2F/Df + Spir::GFP
F
Dendritic Field (mm²)
0.35
0.30
0.25
0.20
**
spir2F/+
spirDf/+
spir2F/Df
spir1/Df
spir2F/Df + Spir::GFP
G
critical value (spir2F/+)
No. of Intersections
70
60
50
40
30
20
10
0
0
100
200
300
400
Distance from soma (µm)
spir2F/+
spirDf/+
spir2F/Df
spir1/Df
spir2F/Df + Spir::GFP
H
Critical Value
70
65
60
55
50
45
40
***
*
spir2F/+
spirDf/+
spir2F/Df
spir1/Df
spir2F/Df + Spir::GFP

Figure 3

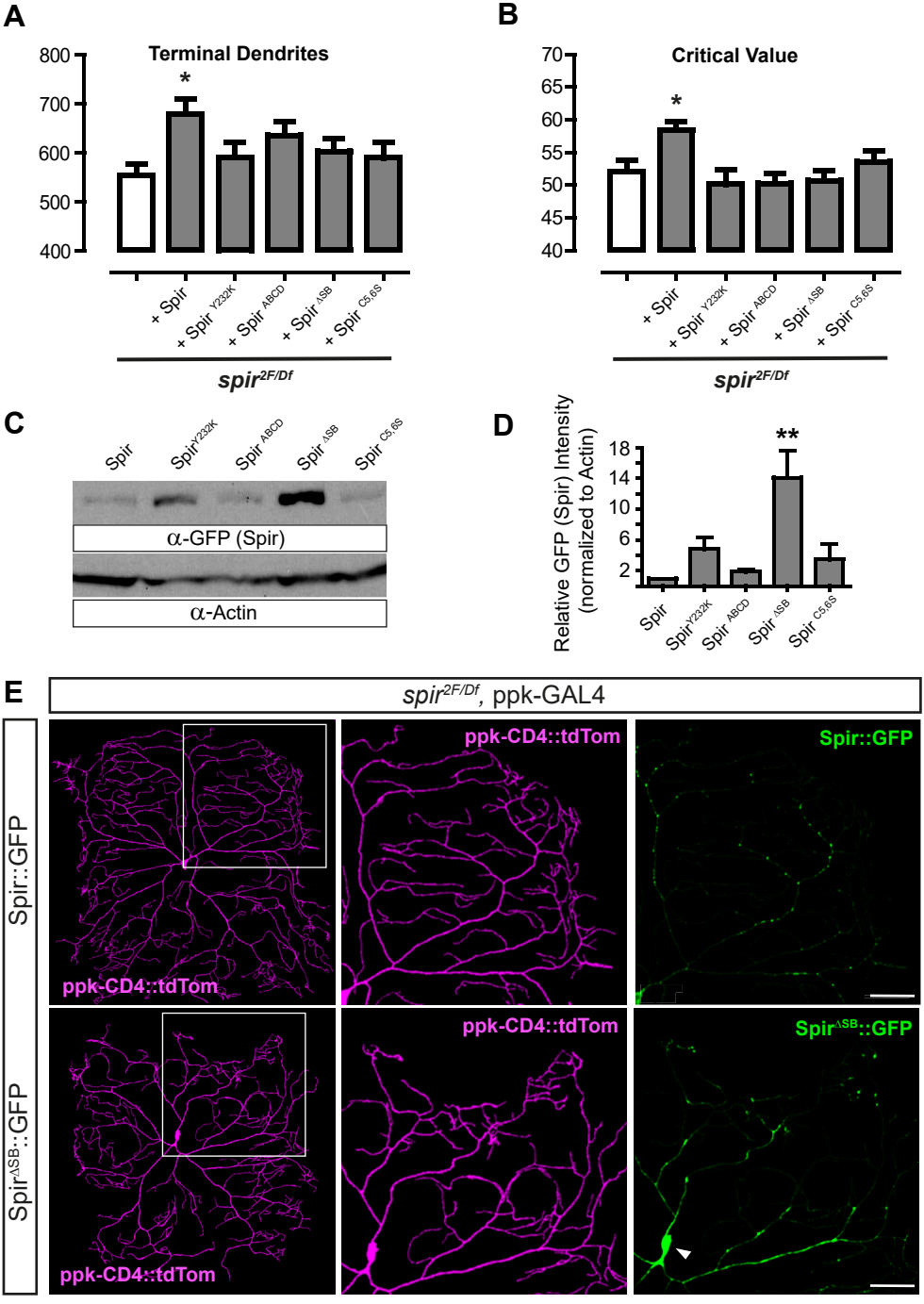
A
Terminal Dendrites
800
700
600
500
400
*
+ Spir
+ Spir Y232K
+ Spir ABCD
+ Spir ΔSB
+ Spir C5,6S
spir2F/Df
B
Critical Value
70
65
60
55
50
45
40
*
+ Spir
+ Spir Y232K
+ Spir ABCD
+ Spir ΔSB
+ Spir C5,6S
spir2F/Df
C
Spir
SpirY232K
Spir ABCD
SpirΔSB
Spir C5,6S
α-GFP (Spir)
α-Actin
D
Relative GFP (Spir) Intensity (normalized to Actin)
18
14
10
6
2
**
Spir
SpirY232K
Spir ABCD
SpirΔSB
Spir C5,6S
E
spir2F/Df, ppk-GAL4
Spir::GFP
SpirΔSB::GFP
ppk-CD4::tdTom
ppk-CD4::tdTom
Spir::GFP
ppk-CD4::tdTom
ppk-CD4::tdTom
SpirΔSB::GFP

Figure 4

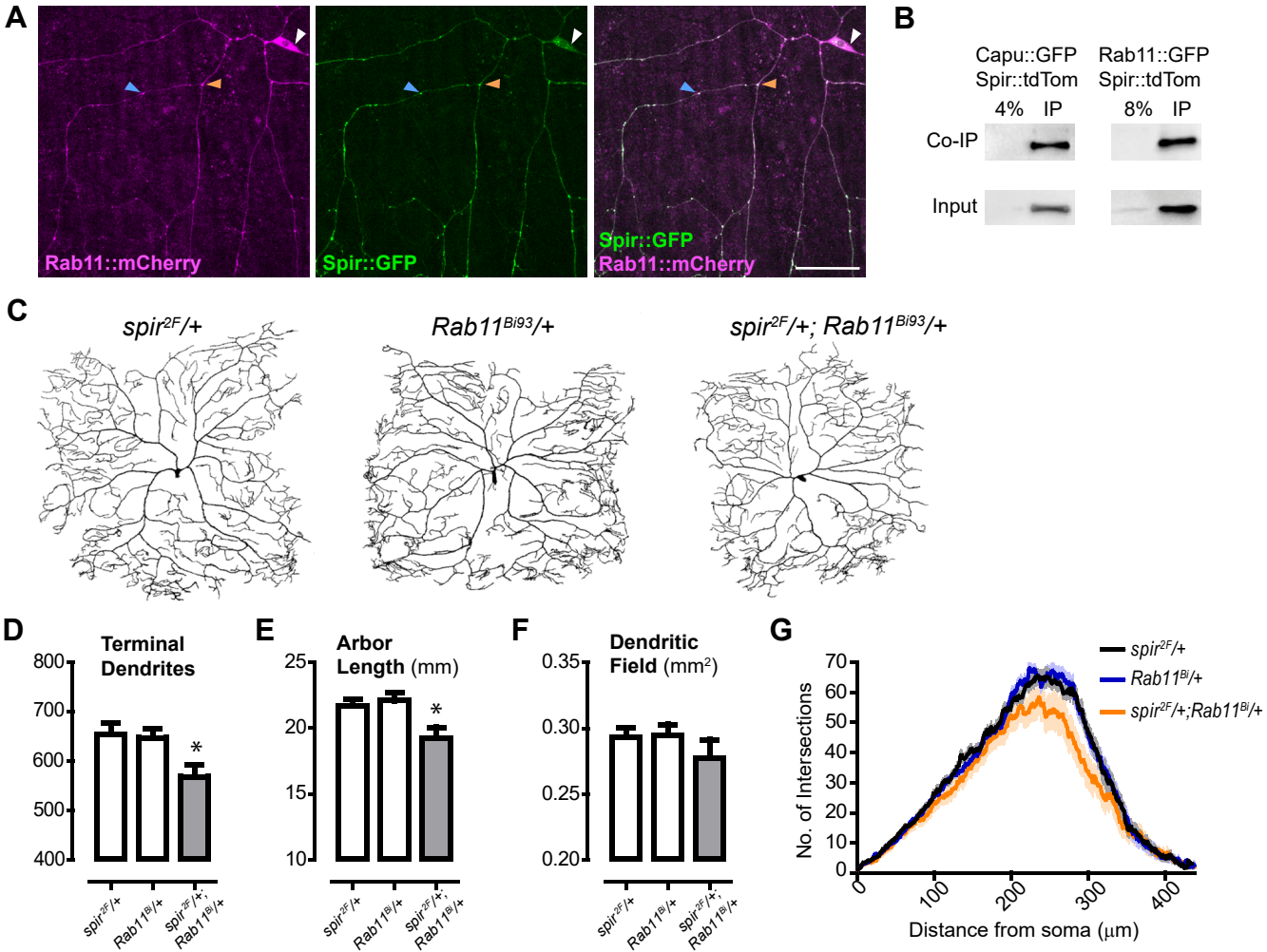
A
Rab11::mCherry
Spir::GFP
Spir::GFP
Rab11::mCherry
B
Capu::GFP
Spir::tdTom
Rab11::GFP
Spir::tdTom
4%
IP
8%
IP
Co-IP
Input
C
spir2F/+
Rab11Bi93/+
spir2F/+; Rab11Bi93/+
D
Terminal Dendrites
800
700
600
500
400
*
spir2F/+
Rab11Bi/+
spir2F/+; Rab11Bi/+
E
Arbor Length (mm)
25
20
15
10
*
spir2F/+
Rab11Bi/+
spir2F/+; Rab11Bi/+
F
Dendritic Field (mm2)
0.35
0.30
0.25
0.20
spir2F/+
Rab11Bi/+
spir2F/+; Rab11Bi/+
G
No. of Intersections
70
60
50
40
30
20
10
0
0
100
200
300
400
Distance from soma (μm)
spir2F/+
Rab11Bi/+
spir2F/+;Rab11Bi/+

Figure S1

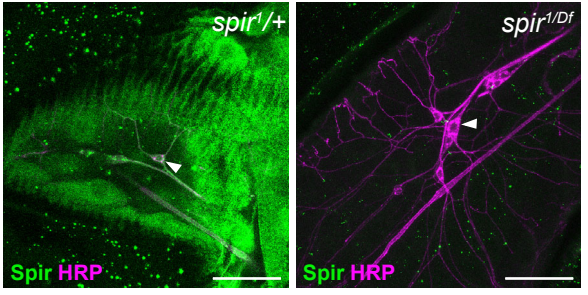

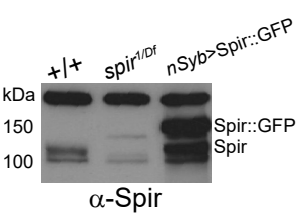

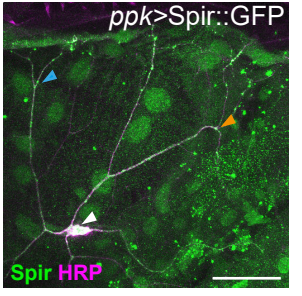

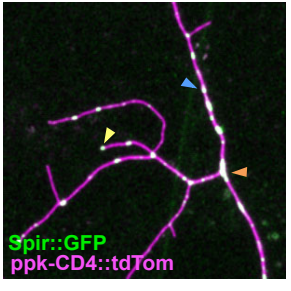

E

Spir::GFP puncta in static images at L3			
	Occurrence		
	Shafts	Branch points	Tips
Spir::GFP occupancy of each location	100%	28%	6%
Proportion of total Spir::GFP puncta at each location	57%	36%	7%

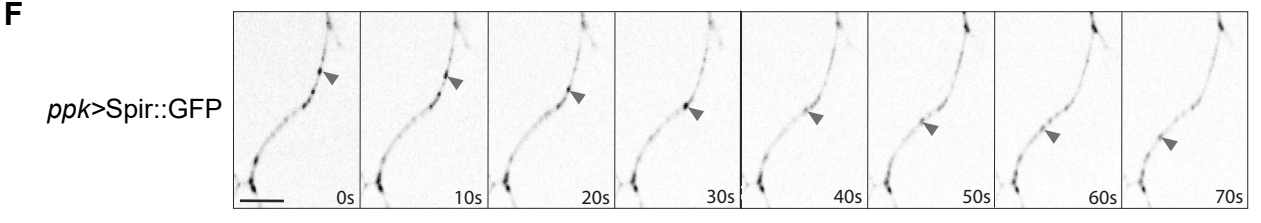

Figure S2

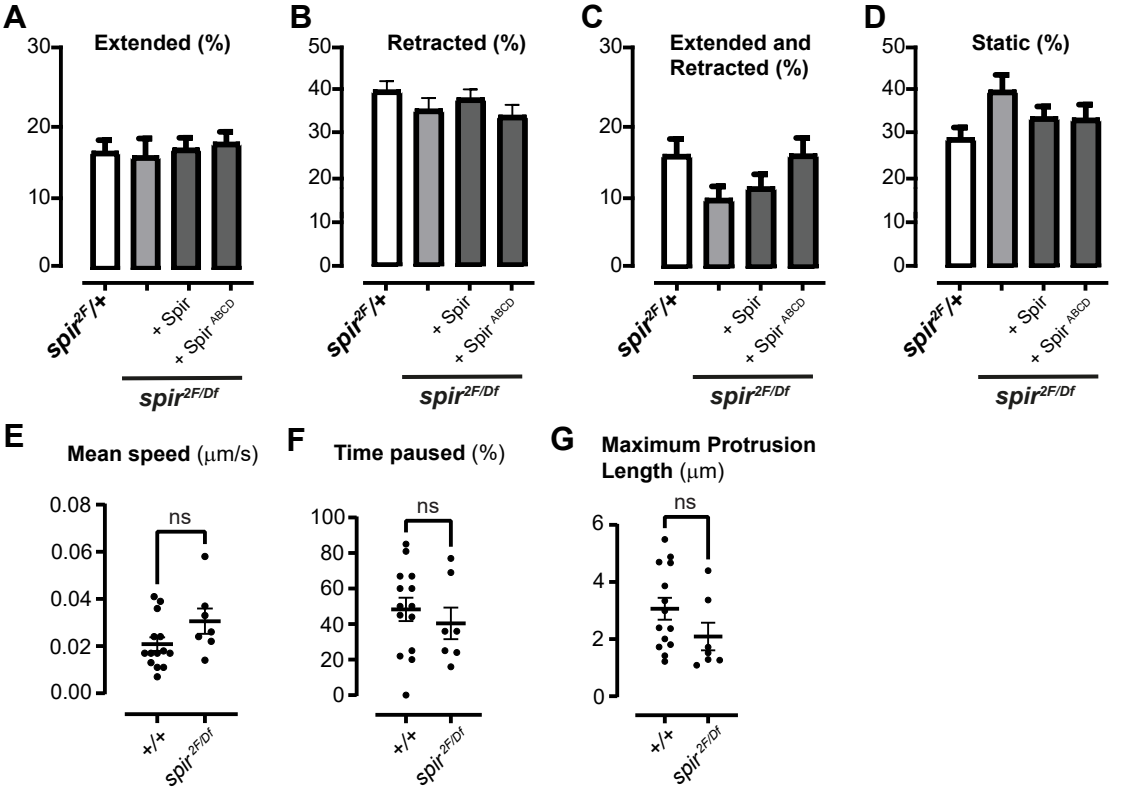
A
Extended (%)
30
20
10
0
spir2F/+
+ Spir
+ Spir ABCD
spir2F/Df
B
Retracted (%)
50
40
30
20
10
0
spir2F/+
+ Spir
+ Spir ABCD
spir2F/Df
C
Extended and Retracted (%)
30
20
10
0
spir2F/+
+ Spir
+ Spir ABCD
spir2F/Df
D
Static (%)
50
40
30
20
10
0
spir2F/+
+ Spir
+ Spir ABCD
spir2F/Df
E
Mean speed (μm/s)
0.08
0.06
0.04
0.02
0.00
ns
+/+
spir2F/Df
F
Time paused (%)
100
80
60
40
20
0
ns
+/+
spir2F/Df
G
Maximum Protrusion Length (μm)
6
4
2
0
ns
+/+
spir2F/Df

Figure S3

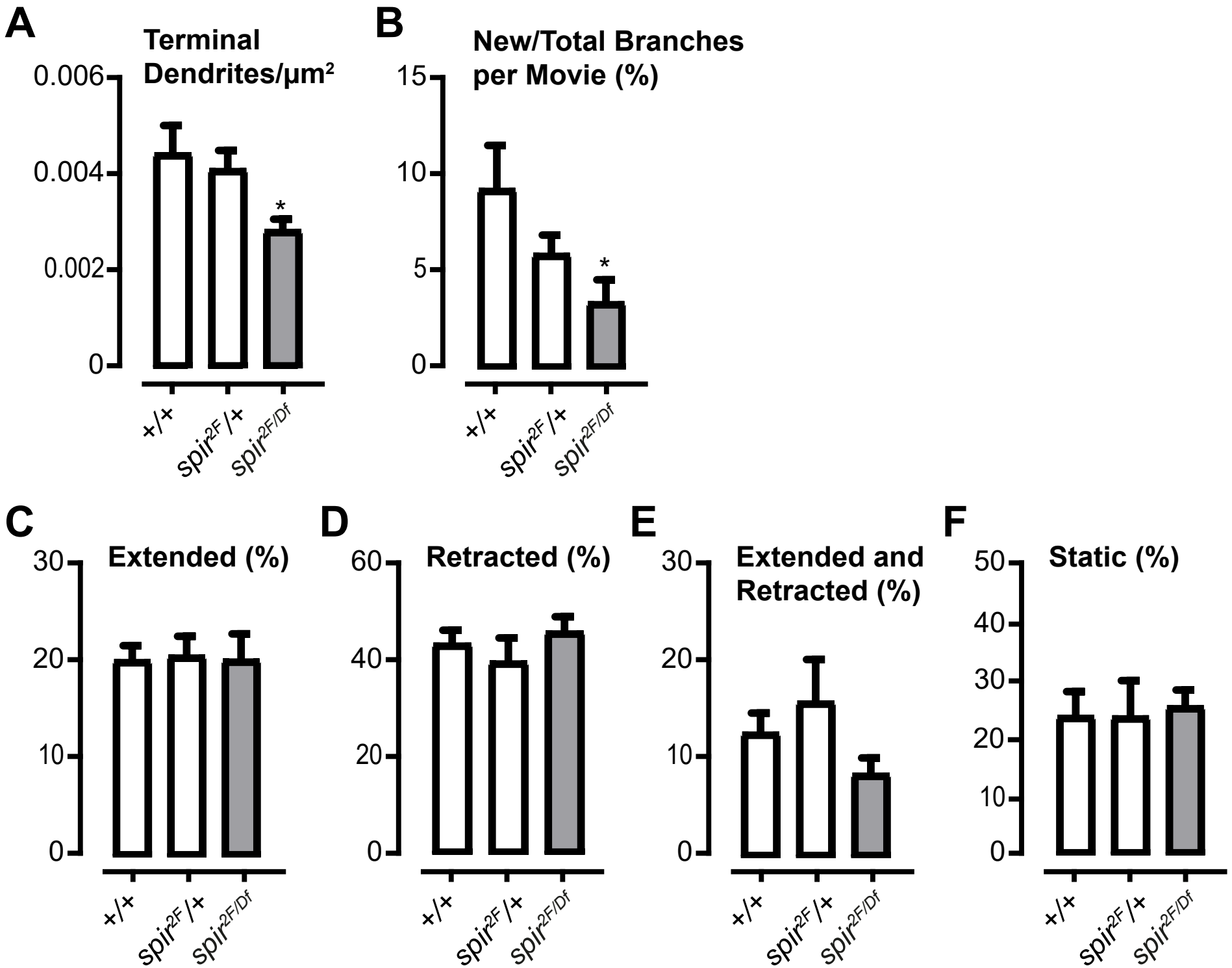
A
Terminal Dendrites/µm²
0.006
0.004
0.002
0
*
+/+
spir2F/+
spir2F/Df
B
New/Total Branches per Movie (%)
15
10
5
0
*
+/+
spir2F/+
spir2F/Df
C
Extended (%)
30
20
10
0
+/+
spir2F/+
spir2F/Df
D
Retracted (%)
60
40
20
0
+/+
spir2F/+
spir2F/Df
E
Extended and Retracted (%)
30
20
10
0
+/+
spir2F/+
spir2F/Df
F
Static (%)
50
40
30
20
10
0
+/+
spir2F/+
spir2F/Df

Figure S4

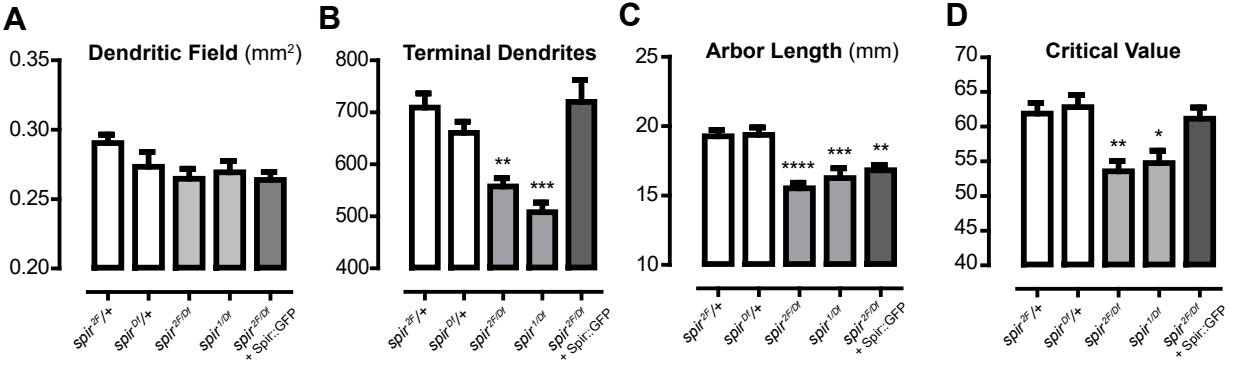
A
Dendritic Field (mm2)
0.35
0.30
0.25
0.20
B
Terminal Dendrites
800
700
600
500
400
**
***
C
Arbor Length (mm)
25
20
15
10
****
***
**
D
Critical Value
70
65
60
55
50
45
40
**
*
spir-2F/+
spir-D1/+
spir-2F/Df
spir-1/Df
spir-2F/Df + Spir::GFP

Figure S5

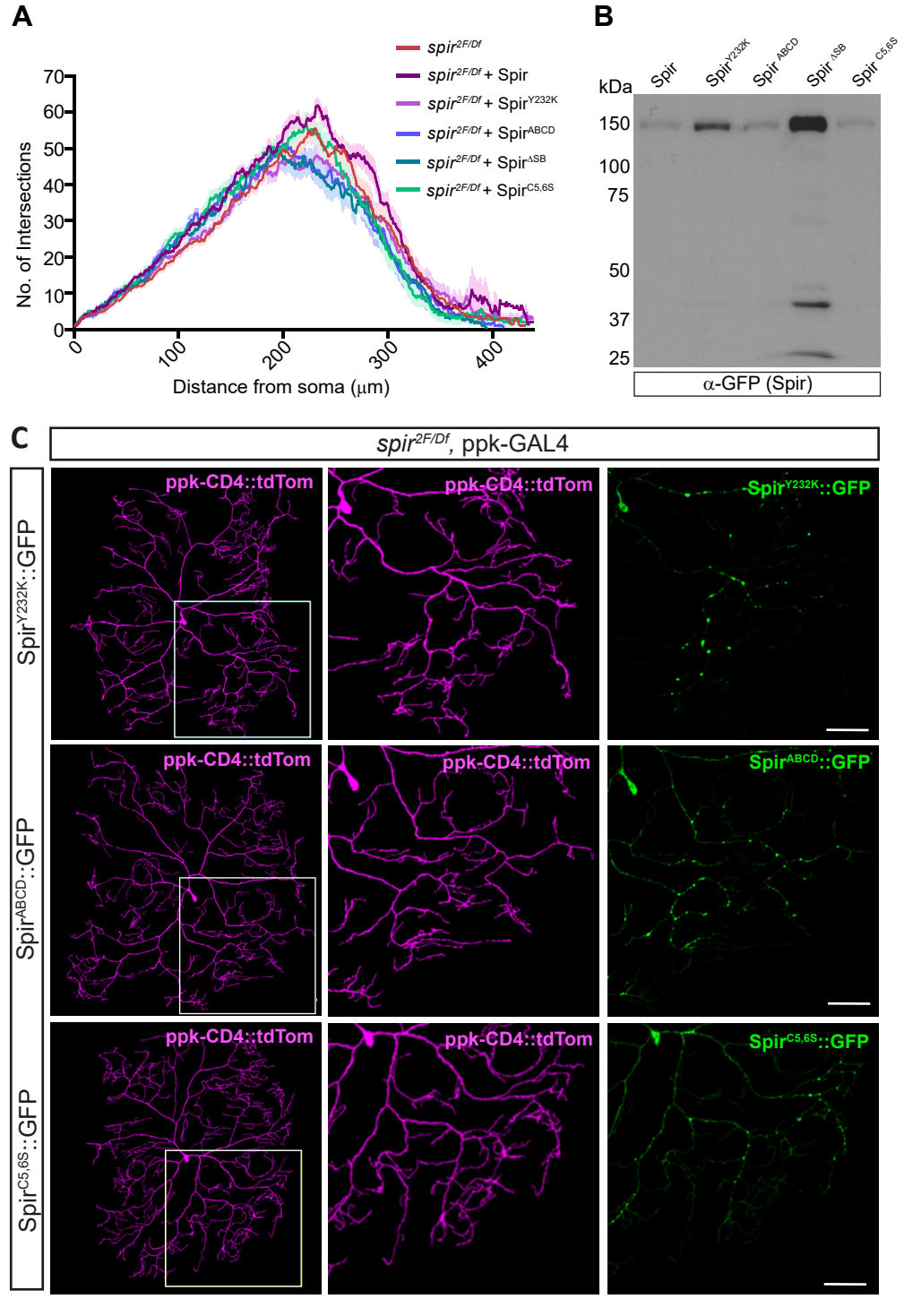
A
spir2F/Df
spir2F/Df + Spir
spir2F/Df + SpirY232K
spir2F/Df + SpirABCD
spir2F/Df + SpirΔSB
spir2F/Df + SpirC5,6S
No. of Intersections
Distance from soma (μm)
B
kDa
Spir
SpirY232K
SpirABCD
SpirΔSB
SpirC5,6S
150
100
75
50
37
25
α-GFP (Spir)
C
spir2F/Df, ppk-GAL4
SpirY232K::GFP
SpirABCD::GFP
SpirC5,6S::GFP
ppk-CD4::tdTom
SpirY232K::GFP
SpirABCD::GFP
SpirC5,6S::GFP

Figure S6

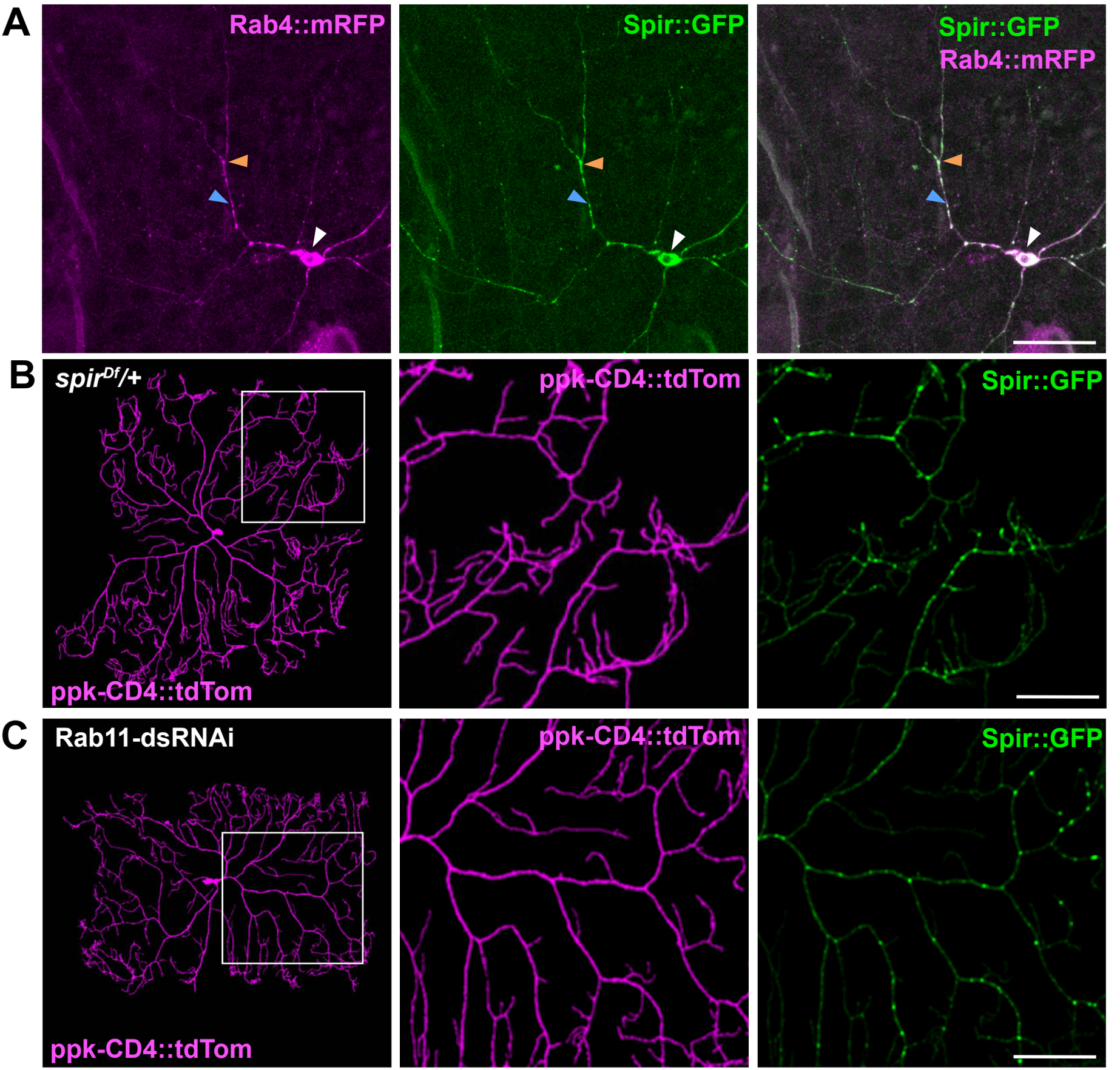
A
Rab4::mRFP
Spir::GFP
Spir::GFP
Rab4::mRFP
B
spirDf/+
ppk-CD4::tdTom
ppk-CD4::tdTom
Spir::GFP
C
Rab11-dsRNAi
ppk-CD4::tdTom
ppk-CD4::tdTom
Spir::GFP